Analysis of Functional Models in Density Functional Theory: Applications to Transition Metal Oxides

A Thesis Submitted to the
College of Graduate Studies and Research
in Partial Fulfillment of the Requirements
for the degree of Master of Science
in the Department of Physics and Engineering Physics
University of Saskatchewan
Saskatoon

By
Tyrel Kerpan

Permission to Use

In presenting this thesis in partial fulfilment of the requirements for a Postgraduate degree from the University of Saskatchewan, I agree that the Libraries of this University may make it freely available for inspection. I further agree that permission for copying of this thesis in any manner, in whole or in part, for scholarly purposes may be granted by the professor or professors who supervised my thesis work or, in their absence, by the Head of the Department or the Dean of the College in which my thesis work was done. It is understood that any copying or publication or use of this thesis or parts thereof for financial gain shall not be allowed without my written permission. It is also understood that due recognition shall be given to me and to the University of Saskatchewan in any scholarly use which may be made of any material in my thesis.

Requests for permission to copy or to make other use of material in this thesis in whole or part should be addressed to:

Head of the Department of Physics and Engineering Physics
116 Science Place
University of Saskatchewan
Saskatoon, Saskatchewan
Canada
S7N 5E2

Abstract

This work presents a study of the electronic structure of four transition metal oxides (TMOs) using spectroscopic data and a variety of theoretical models. TMOs are a class of materials made from *d*-block metals in the periodic table, and one or more oxygen atoms. The nature of *d*-electrons is examined and theoretical models used to treat *d*-electron systems are tested against experimental data.

Background theory of condensed matter physics is outlined. An overview of density functional theory (DFT) as a theoretical model for calculating the electronic structure of materials is presented. A variety of exchange-correlation (XC) functionals used within the DFT framework are outlined and tested for their applicability to the TMO systems in question. X-ray spectroscopy is briefly outlined and used to test the validity of the different XC functionals.

All four compounds, AgO, Ag_2O, CuO, and Cu_2O require a Hubbard U term in the XC functional to most accurately reproduce experimental results. The effects of varying the value of U is examined in depth. The oxygen K-edge X-ray emission spectra (XES) exhibits a"two peak" structure for all compounds; the effect of varying the U value is to change the intensity ratio of the two peaks. The ratio of the two peaks as a function of U shows a linear trend in all compounds. A simple line is fit to the peak ratio vs. U curve. A common line between all compounds would provide an important metric with which to predict the appropriate U value needed in similar materials based on simple experimental data. However, the parameters of the fitted line were not common between the four compounds and any metric derived from this method would be system-dependent and not widely applicable to other systems. There are, however, interesting trends in the data when the U value is varied that provide subjects for future research.

A number of fundamental quantities are determined both from experiment and theoretical calculations. Calculated bandgap values are shown to be lower than the experimental values for most functionals tested. This is not unexpected as DFT methods are known to

predict much smaller bandgaps than expected. The Heyd-Scuseria-Ernzerhof (HSE) functional used for Ag_2O and Cu_2O does predict the bandgaps very accurately. The core-hole effect is estimated and proven to be negligible in these systems. Charge transfer and on-site Coulomb repulsion energies, important quantities in the electronic behaviour of TMOs, are determined and compared to previously reported values.

Acknowledgements

I am very grateful for the support and guidance of my supervisor, Alex Moewes, throughout my time with him. The help of the members of the 'Beamteam' was more than appreciated. I would like to thank John McLeod especially for sharing his wealth of knowledge and guiding me through much of the way. I appreciate the time my committee has taken out of their busy schedules as well.

This research was supported through funding by the Canada Research Chair program and the Graduate Teaching Fellowship program of the University of Saskatchewan.

A treatise much more lengthy than what is to follow would be needed to explain the gratitude I have for the love and support given to me by my wife and parents. Any words written only seem to diminish a description rather than add to it, and so I say simply....

Thank you, I love you.

To Mom, Dad, and Serene — my pillars

Contents

List of Tables

List of Figures

List of Abbreviations

AMF	Around Mean Field
ALS	Advanced Light Source
BGO	Bismuth Germanate, chemical formula $Bi_4Ge_3O_{12}$
BIS	Bremsstrahlung Isochromatic Spectroscopy
BJ	Becke-Johnson
DFT	Density Functional Theory
DOS	Density of States
FP-LAPW + lo	Full Potential Linear Augmented Plane-Wave plus Local Orbital
GGA	Generalized Gradient Approximation
HF	Hybrid Functional
HMF	Hubbard Mean Field
HSE	Heyd-Scuseria-Ernzerhof
KS	Kohn-Sham. Used in Figure 2.1.
LDA	Local Density Approximation
LR	Long Range
MBJ	Modified Becke-Johnson
OPE	Optimized Potential Method
PBE	Perdew-Burke-Ernzerhof
pDOS	Partial/Projected Density of States
SE	Schrödinger Equation. Used in Figure 2.1.
SIC	Self Interaction Corrected
SIE	Self Interaction Error
SR	Short Range
TFY	Total Fluorescence Yield
TM	Transition Metal
TMO	Transition Metal Oxide
XAS	X-ray Absorption Spectroscopy/Spectra
XC	Exchange-Correlation
XES	X-ray Emission Spectroscopy/Spectra
XPS	X-ray Photoelectron Spectroscopy

Chapter 1

Introduction

The electronic structure of solids is a very broad term, yet it can be simply defined as the wavefunctions and energies associated with the wavefunctions of electrons. This definition, however, masks the incredibly complex nature of interactions between electrons and nuclei that govern the wavefunctions in the solid. There are on the order of 10^{23} individual particles that interact with each other to form a solid, and all these interactions contribute to the electronic structure. However difficult, it is of great importance to our daily lives to understand the electronic structure of materials.

The electronic structure governs most properties of materials. Whether it is a conductor of electricity, an insulator, or somewhere in between (semiconductor), its color, hardness, thermal conductivity, optical properties, and magnetic properties to name a few, are all determined by how the electrons and nuclei interact to make up the electronic structure.

An interesting and important class of solids are the transition metal oxides (TMOs). They are formed from the transition metals, shown in Figure 1.1, and oxygen. TMOs exhibit a wide variety of electronic and magnetic properties. Iron has varying magnetic order depending on temperature and pressure. Many TMOs transition between metallic and insulating states. Catalytic properties due to varying oxidation states of the metal are observed. Many are semiconductors with applications in battery and solar cell technologies, and the nature of high temperature superconductors is thought to be correlated with the cuprite structure of late TMOs.

It is not a coincidence that the TMOs which have such a rich variety of properties fall in the "*d*-block" of the periodic table. It is the *d*-electrons, specifically the valence *d*-

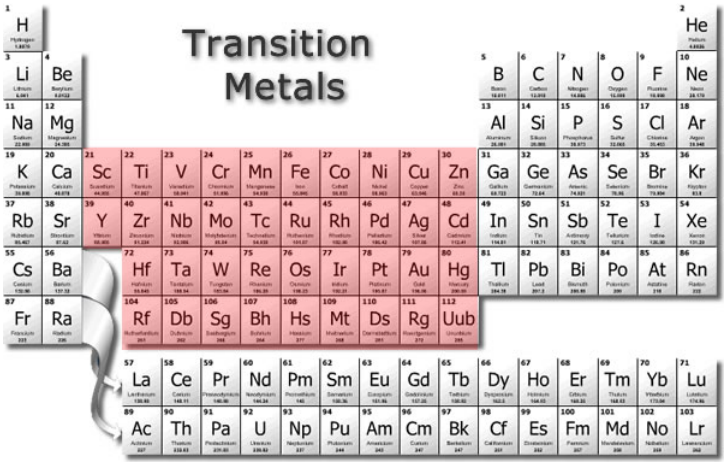

Figure 1.1: The transition metals. Figure from http://media.orvsd.org/FLVS/MASTER_w_images_backup-chemistry-20120216-1404/course_files/flvs/educator_chemistry_v10_gs/module03/03_02b.htm

electrons, which are responsible for the characteristics of TMOs. Understanding the electronic structure of materials is of immense importance to science and technology; it allows us to engineer new materials with desired characteristics, predict the properties of materials not yet made, and furthers theoretical understanding of the fundamentals of materials. Thus, it is important to understand the nature of d-electrons in TMOs. Theoretical models are continuously improving, yet it is still very difficult to model and predict their behaviour.

The total many-bodied Schrödinger equation must be solved in order to theoretically calculate the electronic structure of a solid. This is intractable for any real solid even with modern supercomputers and simplifications must be made. Density Functional Theory (DFT) is a computational model which greatly simplifies solving the many-bodied problem. DFT is a very powerful tool in solid state physics; with it we can investigate and sometimes even predict the structure of many materials. There are a variety of "functionals" employed in DFT designed for different properties being studied. Some functionals are designed to calculate intermolecular interactions, excited states, interatomic forces, bandgaps, correlated systems, etc. DFT performs well for a wide variety of systems but d-systems are still notoriously difficult to model. Some functionals perform better than others for d-systems, but there is yet to be a functional that reliably performs well. This work is concerned chiefly with analysis of the performance of functionals applied to TMOs.

Accurate experimental results are needed to evaluate the performance of any theoretical model. X-ray absorption spectroscopy (XAS) and X-ray emission spectroscopy (XES) allow probing of the electronic structure of materials; they are element and site specific techniques that give detailed information of any element or crystal lattice site desired. The spectra obtained from XAS and XES give an approximation of the partial density of states (pDOS); XES and XAS probe the valence and conduction bands, respectively. Comparing experimental to calculated spectra is a simple and repeatable metric to evaluate theoretical models.

The TMOs studied in this work are CuO, Cu_2O, AgO, and Ag_2O. They are all group 11 TMOs and are oxide type semiconductors. Silver oxides have important applications in battery technologies [2, 3], conducting glasses [4], and antibacterial applications [5]. Ag_2O is also a key component in a candidate compound for novel superconductors [6]. Copper oxides also have applications in battery technology as well as in catalysis [7]. The cuprite structure of Cu_2O is believed to play an important role in the origin of high temperature superconductivity [8]. This class of materials includes both "open" and "closed" d-shell compounds; open shells have unpaired electrons, while closed shells have all electrons paired; this makes these materials of interest, especially their magnetic properties.

This work is organized as follows. An overview of the quantum mechanical theory applicable to condensed matter physics will be presented in order to outline the problem to be solved, namely, solving the many body Schrödinger equation. Density functional theory will be introduced as a theoretical tool for solving this problem. Within DFT, the exchange-correlation energy functional is a critical factor determining the accuracy of any DFT calculation; several of the functionals employed in calculations will be discussed and their merits and applicability to specific systems will be examined. Understanding the electronic structure of transition metal oxides boils down to understanding the nature of d-electrons and their interactions in solids. An examination of the characteristics of d-electrons, specifically their properties in TMOs, will be presented. The principles of X-ray spectroscopy will be briefly reviewed, followed by the experimental and calculational details of this research. The results section will begin with a comparison of calculations with different functionals to experimen-

tal results to determine the most appropriate functional for the compounds studied. All the compounds are best modelled by a PBE+U functional (explained in section 2.5.3 and chapter 7), which leads to the following section of the effects of varying the U value in the exchange-correlation energy functional. An attempt is made to create a semi-empirical method for determining the proper U value needed in calculations based on experimental results. The final section discusses the fundamental quantities that are determined from experiment and calculations and comparison is made to values previously reported in the literature. This thesis will naturally be concluded with a brief section summarizing the conclusions made during the course of this research.

Chapter 2

Background Condensed Matter Theory

2.1 Quantum Mechanics of Condensed Matter Physics

Determining the electronic structure of a material requires solving the complex interaction of the many electrons with themselves and their nuclei. Unfortunately, exact solutions to this problem are intractable for systems more complex than the simple hydrogen atom or H_2^+ molecule. The goal of determining the ground-state electronic structure of a material reduces to finding solutions to the Schrödinger equation:

$$\mathbb{H}\Phi = E\Phi \tag{2.1.1}$$

where Φ is the eigenstate (total ground-state wavefunction to be determined), $\mathbb{H}$ is the total Hamiltonian of the system, and E is the energy eigenvalue of the eigenstate. Once the eigenstates are known it is possible to determine many physical properties by replacing the Hamiltonian operator with the operator of interest.

The full many-bodied Hamiltonian is (in atomic units):

$$\hat{H} = -\frac{1}{2}\sum_i \frac{\nabla^2}{M_i} - \frac{1}{2}\sum_i \frac{\nabla^2}{m_i} - \sum_{i,j} \frac{Z_i}{|\vec{R}_i - \vec{r}_j|} + \frac{1}{2}\sum_{i\neq j} \frac{1}{|\vec{r}_i - \vec{r}_j|} - \frac{1}{2}\sum_{i,j} \frac{Z_i Z_j}{|\vec{R}_i - \vec{R}_j|} \tag{2.1.2}$$

where M and m are the nucleus and electron mass, respectively, Z is the nuclear charge, and $\vec{R}$ and $\vec{r}$ are the nucleus and electron position vectors, respectively.

Defining

$$\hat{T} = -\frac{1}{2}\sum_i \frac{\nabla^2}{m_i}, \quad \hat{T}_n = -\frac{1}{2}\sum_i \frac{\nabla^2}{M_i}, \quad \hat{V}_{nn} = -\frac{1}{2}\sum_{i,j} \frac{Z_i Z_j}{|\vec{R}_i - \vec{R}_j|},$$

$$\hat{V}_{ne} = -\sum_{i,j} \frac{Z_i}{|\vec{R}_i - \vec{r}_j|}, \quad \hat{U}_{ee} = \frac{1}{2}\sum_{i \neq j} \frac{1}{|\vec{r}_i - \vec{r}_j|}$$

the Hamiltonian can be written simply as

$$\hat{H} = \hat{T} + \hat{T}_n + \hat{V}_{nn} + \hat{V}_{ne} + \hat{U}_{ee} \tag{2.1.3}$$

The first and second terms in 2.1.3 are the kinetic energies of the electron and nuclei, respectively, the third and fourth terms are the nuclei-nuclei repulsion and nuclei-electron Coulombic terms, respectively, and the fifth term is the electron-electron repulsion. As stated above, the Schrödinger equation is too difficult to solve with this Hamiltonian and approximations need to be made to solve complex systems.

2.2 Born-Oppenheimer Approximation

The first approximation is the Born-Oppenheimer approximation which decouples the electron and nuclei terms. The nuclei are several orders of magnitude more massive than the electrons and can be approximated as static charges with respect to the electrons and have zero kinetic energy. Thus, $\hat{T}_n$ is zero and $\hat{V}_{nn}$ is a constant. The $\hat{V}_{ne}$ term can be relabelled $\hat{V}_{ext}$ as it is now an "external" potential due to the stationary nuclei. The full many-bodied Hamiltonian 2.1.3 reduces to

$$\hat{H} = \hat{T} + \hat{V}_{ext} + \hat{U}_{ee} \tag{2.2.1}$$

This Hamiltonian is much simpler than the original, however, it is still a many body problem which is too complex to solve. Further approximations such as the Hartree-Fock theory [9], which will not be treated here, attempt to find reasonable approximations to make the problem computationally tractable to solve.

2.3 Density Functional Theory

DFT provides a method of solving the many-bodied problem without solving the Schrödinger equation with the full Hamiltonian. At the heart of DFT are two theorems from Hohenberg and Kohn established in 1964 presented here without proofs [10].

Theorem I: There is a unique one-to-one relation between the external potential $V_{ext}(\vec{r})$ and the electron density $\rho(\vec{r})$.

Corollary: The ground-state expectation value of any observable, such as $\hat{H}$, is a unique functional of the ground-state electron density [11]. This in essence states that the ground-state density holds as much information as ground-state wavefunctions.

Theorem II: The total ground-state energy $E[\rho]$ is a functional of the ground-state density $\rho(\vec{r})$ and is of the form:

$$E[\rho] =< \Phi|\hat{T} + \hat{U}_{ee}|\Phi > + < \Phi|\hat{V}_{ext}|\Phi > \tag{2.3.1}$$

$$E[\rho] = F[\rho] + \int \rho(\vec{r})V_{ext}(\vec{r})d\vec{r} \tag{2.3.2}$$

where $F[\rho]$ is a *universal* functional for any many-electron system, and $E[\rho]$ is variational in that it is minimized by the ground-state density corresponding to V_{ext}.

Corollary II: The functional $F[\rho]$ is independent of any information about the nuclei and is therefore universal for any many-electron system.

In summary, these theorems state that the potential of any system is uniquely defined by the ground-state density, and the total minimum ground-state energy corresponds to the ground-state density. We need only solve for the density since the density holds as much information as the wavefunction. We need only the universal functional $F[\rho]$ to solve the entire problem; unfortunately an explicit expression for $F[\rho]$ is not known. Kohn and Sham provided a method for finding the ground-state density and in turn for solving equation 2.3.2 [12].

2.4 Kohn-Sham Equations

The insight of Kohn and Sham was to map the *real* self-interacting system to an auxiliary system of non-interacting particles. Doing so decouples the complex inter-electron interactions in all but one term of the Hamiltonian while still including these interactions

in one term. This greatly simplifies calculations while still *theoretically* producing the exact ground-state density, thereby solving the *real* problem.

The universal functional can be separated into three terms

$$F[\rho] = T_0 + V_H + V_{xc} \tag{2.4.1}$$

where T_0 is the kinetic energy of the non-interacting electron gas, V_H is the Hartree potential which is due to the classical Coulombic interaction between the electrons, and V_{xc} is the exchange-correlation potential defined as

$$V_{xc} = \frac{\delta E_{xc}}{\delta \rho} \tag{2.4.2}$$

The first two terms in 2.4.1 are known exactly. The exchange-correlation term contains the difference between the exact and non-interacting kinetic energies as well the non-classical effects of exchange and correlation. It is this term that includes the complex inter-electron interactions; it must be formulated and dictates the viability of the entire theory.

Remembering the dependence on ρ, we can write the Hamiltonian for this system as

$$\hat{H}_{KS}[\rho] = \hat{T}_0 + \hat{V}_H + \hat{V}_{xc} + \hat{V}_{ext} \tag{2.4.3}$$

The auxiliary system is made of non-interacting single particles and, therefore, the total ground-state wavefunction for this system can be given exactly by a set of single particle wavefunctions. The density of the N single particle system is constructed from the single particle wave functions $\varphi_i(\vec{r})$ as

$$\rho(\vec{r}) = \sum_{i}^{N} |\varphi_i(\vec{r})|^2 \tag{2.4.4}$$

We can solve relatively simple single-particle Schrödinger equations

$$\hat{H}_{KS}\varphi_i = \epsilon_i \varphi_i \tag{2.4.5}$$

once $\hat{H}_{KS}[\rho]$ is known.

Equations 2.4.3, 2.4.4, and 2.4.5 are the Kohn-Sham Equations which can be solved iteratively. First an initial guess for the density ρ_0 is made and put into equation 2.4.3. The Hamiltonian $\hat{H}_{KS_0}$ is formed and put into equation 2.4.5 to give the set of φ_i. Finally the φ_i are used in 2.4.4 to give a new density ρ_1. The cycle continues until a final self-consistent density is found. This final density is said to be consistent with the Hamiltonian and is the ground-state density of the real system. A figure outlining the principles of DFT is shown below.

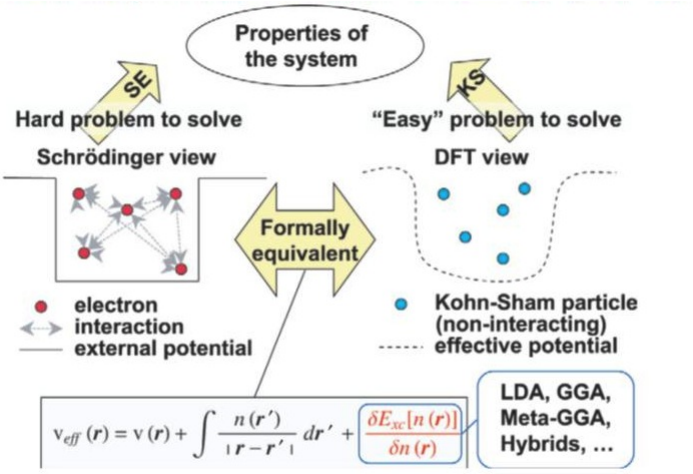

Figure 2.1: The principles of DFT. Image modified from http://nanohub.org/resources/13466/download/2011.11.14-Sinnott.pdf

Up to this point the Kohn-Sham approach is exact except for the Born-Oppenheimer approximation. The electronic structure of most materials could be solved very accurately if the exchange-correlation term were known exactly. The problem at this stage is that we do not yet know the exchange-correlation term, particularly, one that accurately models *d*-systems.

2.5 Exchange-Correlation Functional

The exchange-correlation functional (also referred to as the XC energy, as the expectation value of the functional produces the energy) is the most important factor in the

applicability of DFT. There are numerous different functionals each with its focused application, advantages, and disadvantages. However, every one can be written in the same general form

$$E_{xc}[\rho(\vec{r})] = \int \rho(\vec{r})\varepsilon_{xc}(\vec{r})d\vec{r} \tag{2.5.1}$$

where $E_{xc}[\rho(\vec{r})]$ is the total XC energy, and $\varepsilon_{xc}(\vec{r})$ is the XC energy density. In essence, different functionals can be characterized by the way they sample the density surrounding each electron in order to construct $\varepsilon_{xc}(\vec{r})$.

The XC effects are quantum-mechanical in nature. In general, the exchange interaction dominates the XC energy and is due to the Pauli exclusion principle and the antisymmetric nature of the total system wavefunction; correlation is due to repulsion between electrons. The effect is that electrons tend to repel each other more than the classical Coulomb repulsion. The exchange part can in fact be handled analytically if the correlation is ignored; this is the basis of Hartree-Fock theory. However, the correlation contribution can be significant in some cases and must be included in a complete treatment of the system.

A very important concept is the exchange-correlation hole $n_{xc}(\vec{r}, \vec{r\prime})$. The effect of the XC hole is to reduce the classical probability of finding an electron at position $\vec{r\prime}$ due to an electron being at position $\vec{r}$. Harris highlighted the importance of the XC hole with his adiabatic connection approach to defining the XC-energy [13]. The simple result for the XC-energy density

$$\varepsilon_{xc}(\vec{r}) = \frac{1}{2}\int \frac{n_{xc}(\vec{r}, \vec{r\prime})}{|\vec{r} - \vec{r\prime}|}d\vec{r\prime} \tag{2.5.2}$$

when inserted in 2.5.1 gives

$$E_{xc}[\rho(\vec{r})] = \frac{1}{2}\int \rho(\vec{r})d\vec{r}\int \frac{n_{xc}(\vec{r}, \vec{r\prime})}{|\vec{r} - \vec{r\prime}|}d\vec{r\prime} \tag{2.5.3}$$

Simply put, if $n_{xc}(\vec{r}, \vec{r\prime})$ is known, the entire many-bodied problem would be solved [11]. In practice, the XC energy density $\varepsilon_{xc}(\vec{r})$ is the quantity considered in the literature. Attention is now turned to a discussion of XC functionals.

2.5.1 Local Density Approximation

The most basic functional is the Local Density Approximation (LDA) proposed by Hohenberg and Kohn in their pioneering paper [10]. The XC energy density is approximated as that of a homogeneous electron gas of the same density as the real system, $\varepsilon_{xc}^{HOM}(\rho[\vec{r}])$. The LDA form of 2.5.1 is

$$E_{xc}^{LDA}[\rho(\vec{r})] = \int \rho(\vec{r})\varepsilon_{xc}^{HOM}[\rho(\vec{r})]d\vec{r} \tag{2.5.4}$$

ε_{xc}^{HOM} for the homogeneous electron gas is known numerically, is a reasonable starting guess and LDA performs reasonably well for systems with slowly varying density. The next step in the advancement of the XC energy functional was to incorporate the gradient of the density.

2.5.2 Generalized Gradient Approximations

The addition of the dependence on the density-gradient was pioneered by Perdew et al. [14, 15, 16]. The density gradient can be incorporated into an enhancement factor that modifies ε_{xc}^{HOM}. The general form can be written as [16]

$$E_{xc}^{GGA}[\rho(\vec{r})] = \int \rho(\vec{r})\varepsilon_{xc}^{HOM}[\rho(\vec{r})]F_{xc}[\rho(\vec{r}), \bigtriangledown\rho(\vec{r})]d\vec{r} \tag{2.5.5}$$

The most popular Generalized Gradient Approximation (GGA) functional was developed by Perdew, Burke, and Ernzerhof and is known as PBE [16]. It treats the exchange and correlation parts of F_{xc} differently and uses no experimentally determined parameters other than the ones involved in ε_{xc}^{HOM}. PBE performs well for a wide variety of systems and is probably the most broadly used functional.

In general, PBE and LDA perform very well for many systems. However, they fail at predicting certain electronic properties of some systems, particularly, highly correlated systems such as the *d*-system TMOs. In general, the *d*-electrons should be localized (strongly correlated), while LDA and GGA tend to delocalize these. There is a self-interaction error (SIE) that is inherent in LDA and GGA functionals that is believed to be the cause of the deficiencies [17, 18]. Furthermore, these functionals systematically underestimate the

bandgap of semiconductors [19, 20]. Functionals have been developed that perform better for the d-systems studied here.

2.5.3 LDA+U

As mentioned above, systems with highly localized electrons (d- and f- electrons in transition metal and rare earth oxides, respectively) are poorly handled by standard LDA and GGA functionals. Systems with only partially filled d-shells are particularly troublesome. Simply put, the d-electrons should be more localized to the host nuclei than LDA and GGA predict. The correction to this problem is the use of orbital dependent potentials, that is, different potentials for different electron orbitals, s, p, d, etc. It should be mentioned here that the name LDA+U is the common name for this functional, however, GGA+U is the same as LDA+U but with the use of GGA correlation rather than LDA correlation. The term PBE+U will be used here as the PBE correlation is used in +U calculations.

The electrons are separated into two subsystems: localized d-electrons and delocalized s- and p- electrons. The s and p electrons are treated with the standard PBE orbital-independent potentials, while the d-electrons have an additional potential term added that serves to localize them to their host atom. There are three main variants of the PBE+U method:

- **HMF**: The Hubbard Mean Field employs the use of the local Hubbard potential in an otherwise mean field [20].
- **SIC**: The approximate Self Interaction Corrected model, as the name suggests, includes an approximate correction to the self interaction effects. It is usually best suited for highly correlated systems [21].
- **AMF**: The Around Mean Field approach is usually better suited for less-strongly correlated systems [22].

The use of PBE+U type functionals for TMOs has been shown to greatly improve calculated electronic properties such as oxidation energies, magnetic moments, and bandgaps [23, 24, 25]. The +U term is somewhat of an ad hoc factor; the exact value of U is often

determined empirically, however, there are some proposed analytical methods with varying success for different systems [26]. A main focus of this research is to determine suitable U values for the studied systems and to possibly develop a reliable analytical method for predicting proper U values for this class of materials.

2.5.4 Hybrid Functionals

A predecessor of DFT that was not treated here is Hartree-Fock theory . Hartree-Fock uses the *exact* exchange energy but does not account for correlation at all. Becke proposed using a portion of the exact HF exchange energy along with conventional GGA correlation [27, 28]. The general form is

$$E_{xc}^{Hyb}[\rho] = E_{xc}^{GGA}[\rho] + \alpha[E_x^{HF}[\phi_{sel}] - E_x^{GGA}[\rho_{sel}]] \tag{2.5.6}$$

The parameter α is a semi-empirical constant determined by fitting of experimental data, ϕ_{sel} are the selected orbitals to which the exact exchange is applied (correlated d-electrons), and ρ_{sel} is the density of the selected electrons. Applying this exact exchange to localized electrons has the same general effect as PBE+U, that is to localize and better handle correlated electrons. The benefits of hybrids over the +U scheme is that there are no system dependent parameters to choose (such as the U value). I will use the label HF for this functional.

2.5.5 Modified Becke-Johnson

As mentioned, LDA and GGA severely underestimate bandgaps. Becke and Johnson developed a method based on the Optimized Potential Method (OPE), which is a computationally very demanding method but does greatly improve bandgap predictions. They constructed a relatively simple model for the exchange term that produces similar bandgaps as expensive OPE [29]. GGA or LDA correlation is used in conjunction with the BJ exchange. Tran and Blaha modified the BJ functional (MBJ) which further improved predicted bandgaps and is the form used in this research [30]. It is also possible to add a U term to d-electrons and form the MBJ+U functional which will also be tested.

2.5.6 Heyd-Scuseria-Ernzerhof (HSE)

The exact HF exchange interaction is inherently long range, and is highly system dependent. Hybrid calculations discussed above can implement the exact HF exchange to selected orbitals relatively efficiently; however, to apply it to the entire system would make the calcu-

lation intractable. To circumvent this problem, the HF exchange can be screened. The HSE functional partitions the full $\frac{1}{r}$ Coulomb potential into short (SR) and long (LR) range parts. The extent of the interaction can be tuned by adjustable parameters. The general form of the functional is

$$E_{xc}^{HSE}(\omega) = E_x^{HSE,SR} + E_x^{PBE,LR}(\omega) + E_c^{PBE} \tag{2.5.7}$$

where

$$E_x^{HSE,SR} = \frac{1}{4}E_x^{Fock,SR}(\omega) + \frac{3}{4}E_x^{PBE,SP}(\omega) \tag{2.5.8}$$

Thus, a fraction ($\alpha = \frac{1}{4}$) of exact Fock exchange is added to the PBE functional only in the short range part, while the long range part is represented by the PBE functional. The screening parameter ω determines the partition into SR and LR terms [28]. The HSE functional has been shown to produce more accurate structural properties and bandgaps than traditional PBE methods for many metallic and semiconductor systems [28, 31, 32].

Chapter 3

The Nature of d-Electrons and Correlated Materials

The topic of d-electrons is far too complex to adequately treat in a short chapter such as this. Only the principles that are pertinent to this research will be discussed, and even these will be treated succinctly. For a much more thorough discussion the reader is directed to reference [1], an excellent book from which much of this chapter is derived.

Transition metals (TMs) are located in the d-block of the periodic table and it is the valence d-electrons that give the rich variety of characteristics to TMs and their compounds. The electronic configuration of most TMs can be written as $[\mathrm{NG}]ns^2(n-1)d^x$, where [NG] denotes the configuration of the preceding noble gas. Since there are five d-orbitals, each of which can contain two electrons of opposite spin, x can range between 1-10. The interaction of these electrons with themselves and with electrons of neighbouring atoms in solids is a complex matter. There are several theoretical frameworks to model the interactions; single particle models, band theory (semi single particle theories such as the LDA of DFT), Hubbard model, molecular orbital theory, ligand field theory, etc. Rather than attempt to outline each model, key concepts will be taken from each and put together to form the framework appropriate for this study.

The importance of the key concepts is such that they need be mentioned first, introduced and defined, and finally tied together in a synoptic fashion. The concepts are:

- Charge Localization
- Itinerant Character

- Orbital overlap
- Bandwidth/Charge Hopping
- On-site Coulomb Repulsion (Hubbard U)
- Correlated Materials
- Charge Transfer
- Charge Transfer vs. Mott-Hubbard Insulators

3.1 Charge Localization

We will start this discussion with an isolated hydrogen-like atomic picture in order to define charge localization. Solutions to the Schrödinger equation in elementary quantum mechanics demands four quantum numbers: the principle quantum number n denotes the shell, ℓ is the orbital angular momentum (or the azimuthal quantum number), m is the magnetic quantum number, and m_s is the spin. The angular momentum number ℓ separates the primary shell into subshells with $\ell = 0, 1, 2, 3...$ labelled $s, p, d, f...$ etc. Each orbital, s, p, d, f, etc. has its own characteristic shape. The $3d$ orbitals (n=3, ℓ=2) are shown in Figure 3.1. The labels e_g and t_{2g} for the orbitals on the left and right respectively will become apparent in a later discussion of molecular orbital theory.

Figure 3.1 shows the angular part of the total wavefunction, which is composed of a radial component and the angular component. Figure 3.2 shows the radial probability distribution for the first few hydrogen-like wavefunctions. What is plotted is proportional to the square of the radial wavefunction. The important thing to take from this graph is that the d electrons reside nearer the nucleus than s or p electrons. There are also no nodes in the $3d$ function which makes these electrons even more likely to be tightly bound to the nucleus. Thus, d-electrons are highly localized. Note that this is an isolated atomic view, yet d-electrons maintain their localized nature in solids as well.

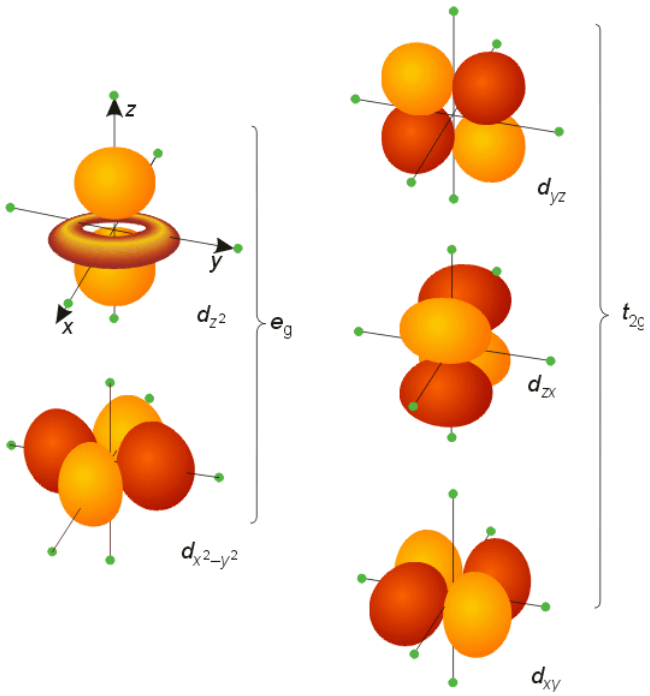

Figure 3.1: 3*d*-orbitals. Image acquired from
http : *//hedberg.web.cern.ch/hedberg/c/atomic*$_t$*heory/2*$_a$*tomic*$_t$*heory*$_h$*l.htm*

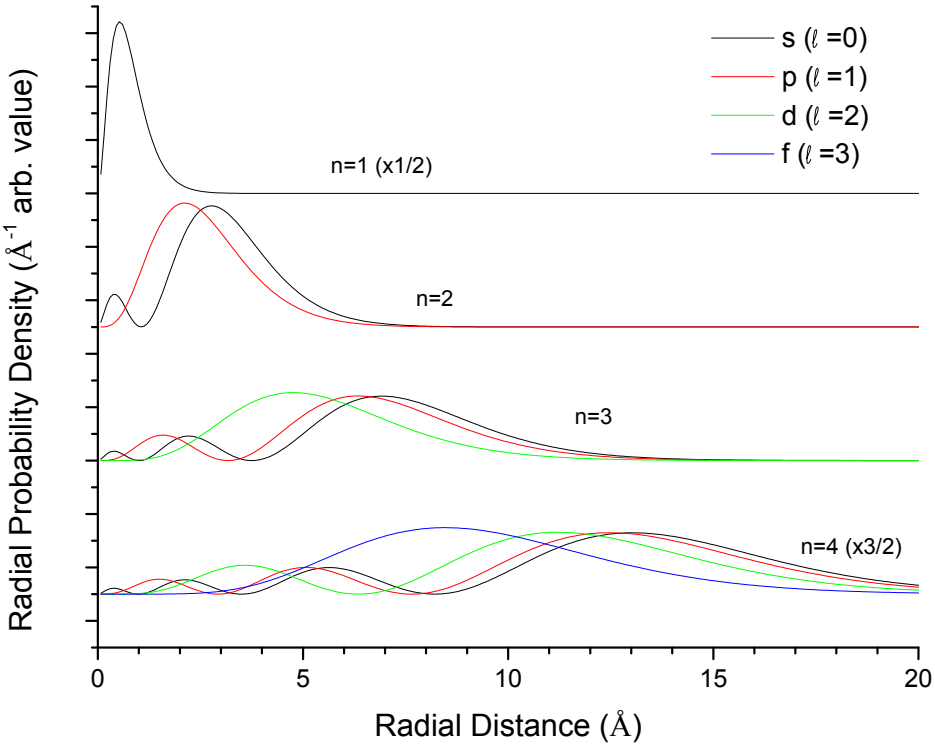

Figure 3.2: Radial probability distribution of hydrogen wavefunctions. Note that the n=1 and n=4 functions have been scaled by 1/2 and 3/2 respectively.

3.2 Itinerant Character, Orbital Overlap, and Bandwidth

When atoms are brought together to form solids, regardless of the bonding nature (ionic, covalent, or metallic), there will be some degree of orbital overlap between orbitals of different atoms. Without delving into the theory of band structure, the amount of overlap between orbitals is related to the hopping integral, the probability that an electron will "hop" from one atom to the other. The greater the overlap, the greater the hopping integral and the probability that electrons will behave itinerantly. For the present purposes it is only necessary to understand that the amount of orbital overlap is proportional to the hopping integral, which is a measure of the itinerant behaviour of electrons in solids. Furthermore, the hopping integral, often labelled t in the literature, is proportional to the bandwidth, labelled W. The bandwidth is the quantity used most frequently and will be used here. The greater the bandwidth of a given symmetry (s, p, d, etc.), the more itinerant electrons will behave. One-electron theories such as band theories and the LDA approach favour itinerant behaviour. In such theories, each electron is treated independently of each other, as if it were in a somewhat averaged potential. They do not treat the interatomic interactions, called correlation effects, effectively.

3.3 On-site Coulomb Repulsion

The on-site Coulomb repulsion energy is defined as "the energy it costs to create a positive and a negative ion from two neutral atoms on sites i and j, according to" [1]

$$E[d_i^n] + E[d_j^n] + U = E[d_i^{n-1}] + E[d_j^{n+1}] \tag{3.3.1}$$

where $E[d_i^n]$ represents the total energy of an atom at site i with a valence configuration d^n, and U is the Coulomb energy. This definition can well apply to any subshell, the d-subshell is used here as an example. It is simply a measure of the energy cost of having two electrons on the same site with the same orbital angular momentum, hence, the term on-site Coulomb repulsion. The term Hubbard U is often used as Hubbard pioneered work on the subject [33].

In summation, the Hubbard U acts as a penalty to itinerant behaviour and favours localized behaviour. This is the origin of the +U term in PBE+U functionals. It is an added term that acts to localize the d-electrons.

3.4 Correlated Materials

Correlated materials can be defined broadly with terms discussed above. Simply put, a highly correlated material has $U \gg W$. That is, the Hubbard U is much greater than the bandwidth. Recalling the definitions of the two, a correlated material is one in which interelectron interactions (U) are more intense than the itinerant nature (of which W is a measure). TMOs are generally classified as strongly correlated materials as the localized d-electrons have strong on-site Coulomb repulsion. The application of the above concepts to TMOs has been beautifully summarized by Stöhr and Siegmann. The context of the quote below is the question of why many TMOs are insulators rather than conductors as band theory predicts:

> ...for the transition metal oxides one can no longer think in the ground-state-like picture of the band model, where the transport [of electrons through the crystal lattice] can easily be envisioned by small excitations around the Fermi level. Obviously, in an insulator higher energy excitations are required to transport an electron through the lattice. Hence one needs to consider excited states that lie above the ground-state by energies up to several eV. The insulator problem therefore boils down to understanding the nature of excited states!
>
> Such large energy excitations are intimately linked to the Coulomb repulsion, i.e., the Hubbard U, when an electron is removed from one atomic site and added to another. Any electron motion through the crystal, which may be envisioned as hopping from metal to oxygen to metal etc., where the hopping parameter is proportional to the band width W, has to overcome the U on a given metal site. One thus obtains an insulator if $U \gg W$. The relative size of these two quantities also serves as a criterion whether a material is correlated ($U \gg W$) or not ($W \gg U$) [1].

3.5 Charge Transfer

The concept of charge transfer is best discussed in the framework of molecular orbital theory. Figure 3.3 shows the situation of a central metal atom surrounded by six oxygen atoms in an octahedral environment. The O p and metal d orbitals mix to form bonding and antibonding molecular orbitals according to the phase of the overlapping lobes, represented by the shade in the figure. The first thing to note about the inset in the top right of the figure is the meaning of the labels e_g and t_{2g}. Recalling Figure 3.1, the five d-orbitals are classified into two sub-groups, e_g and t_{2g}, based on the direction they point with respect to the Cartesian coordinate axis. The e_g have lobes directed along the axis, while the t_{2g} have lobes directed between the axis. When ligands (oxygen in this case) are brought in along these axis, the energies of the two sub-groups become non-degenerate as the field of the ligands effect the electrons in the e_g and t_{2g} differently, shifting the former higher in energy, and the later lower. This is the essence of crystal field theory of which ligand field theory is an extension. This ligand field splitting can be ignored for the current purpose; we will focus on the bonding and antibonding orbitals.

In Figure 3.3 it is assumed that the O p atomic states are lower in energy than the metal d-states. The composition of the bonding and antibonding states depends on the amount of hybridization between the O p and metal d-states. If there is weak hybridization then the lower energy bonding states will be mostly oxygen-like and the antibonding more metal d-like as indicated in the figure. Now, if we ignore the splitting into e_g and t_{2g} states the bonding and antibonding states are separated by an energy labelled Δ_c as in the lower left inset of the figure. This is the charge transfer energy: the energy of an excitation from an oxygen-like bonding state to a metal-like antibonding state. It is defined as

$$E[d^n O] + \Delta_c = E[d^{n+1} O^{-1}] \tag{3.5.1}$$

where $E[d^n O]$ is the ground-state energy of the filled bonding state and $E[d^{n+1} O^{-1}]$ the energy of the excited state with a hole in the oxygen-like bonding state and an electron added to the d-like antibonding state. This charge transfer energy is very important to the classification of TMOs.

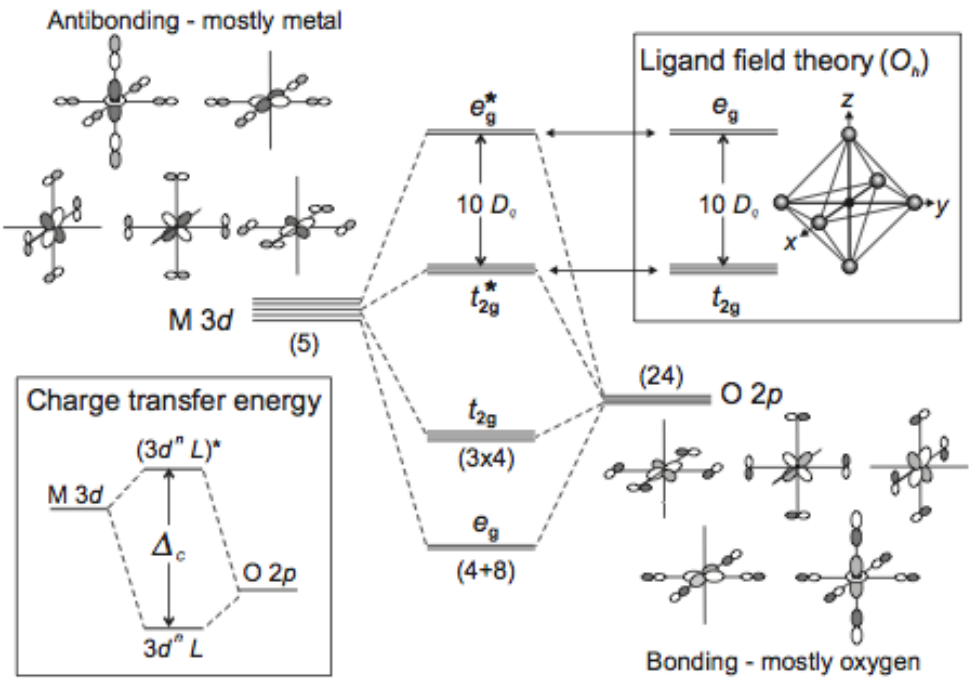

Figure 3.3: Molecular orbital theory for a metal atom octahedrally coordinated by O atoms. Image adapted from reference [1].

.

3.6 Charge Transfer vs. Mott-Hubbard Insulators

Seminal work on the classification of TMOs was performed by Zaanen, Sawatzky, and Allen who determined that the electron excitation processes are governed by two fundamental quantities, the intraatomic Coulomb energy U and the charge transfer energy Δ_c [34]. The two classifications are:

- Mott-Hubbard compounds which have $\Delta_c > U$ so the insulating gap is determined by U, and
- Charge transfer compounds with $U > \Delta_c$, where the gap is determined by Δ_c.

The Mott-Hubbard class is visualized in Figure 3.4. On the left the process of electron transport from one metal atom to another costing an energy U is shown. The central diagram shows that the lowest lying excited states are the ionic states associated with metal-to-metal charge transport with the excited states associated with charge transfer are at higher energy.

The density or states picture on the right shows the energies of the excited configurations relative to the Fermi level $E_F = 0$, where the gap is is determined by U.

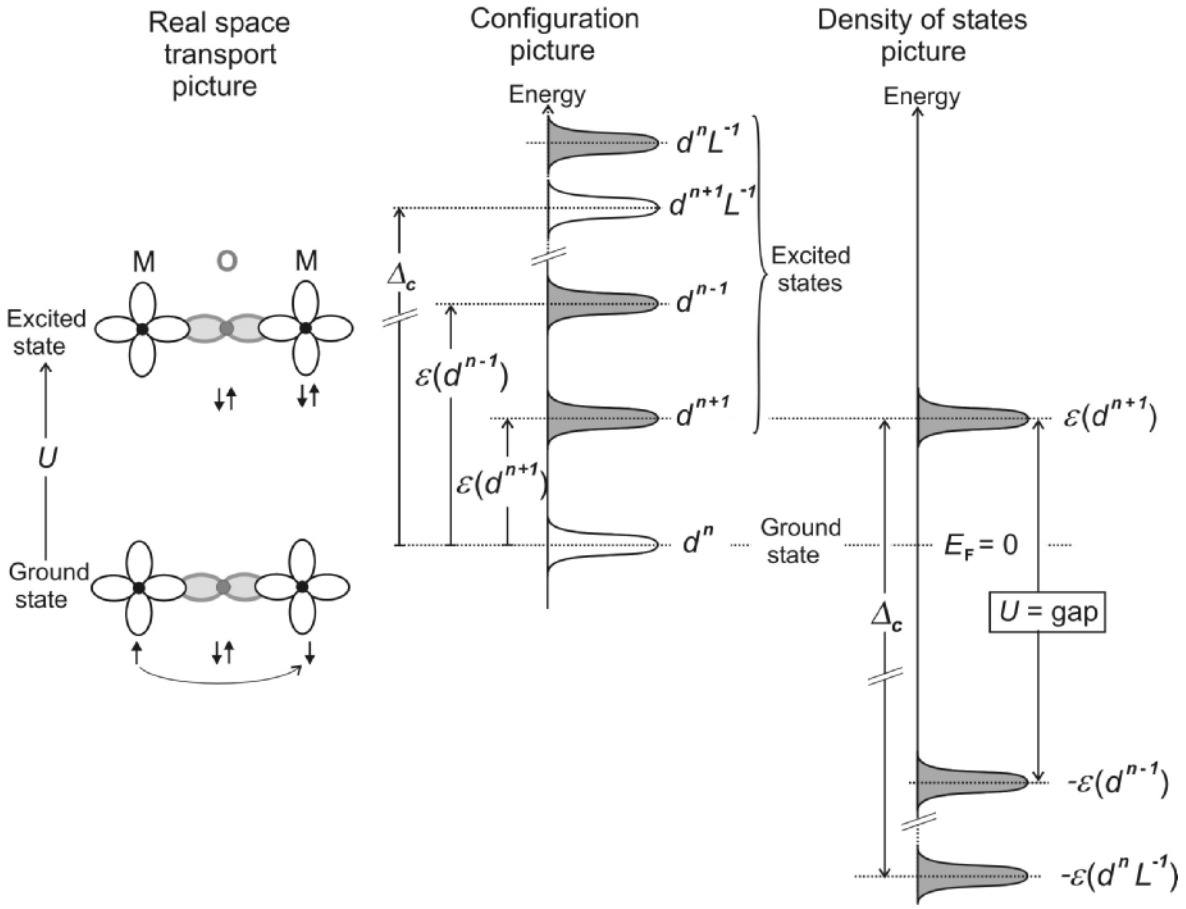

Figure 3.4: Mott-Hubbard Insulator. Image adapted from [1].

The charge transfer case is shown in Figure 3.5. The transport now involves moving an electron from an oxygen to a distant metal atom costing an energy Δ_c. The lowest lying excited state is now the $d^n L^{-1}$ with higher states including metal ions. The view on the right shows the gap is determined by the charge transfer energy Δ_c.

Kurmaev et al. have shown that charge transfer energies of some TMOs can be determined from O 1s XAS and O $K\alpha$ XES by taking the energy difference between the lowest energy XAS peak and the highest XES peak [35]. This is another example of the flexibility of soft X-ray spectroscopy that will be exploited in this research.

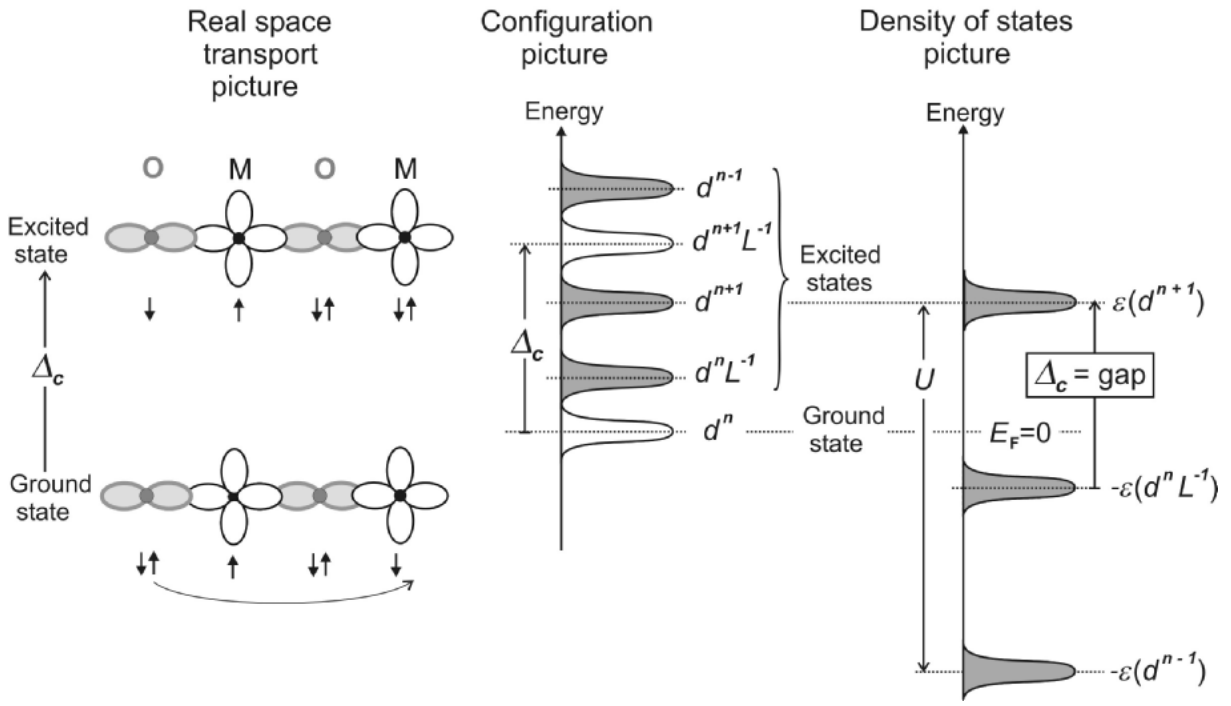

Figure 3.5: Charge Transfer Insulator. Image adapted from [1].

To summarize the complexity of behaviour of d-electrons and TMOs we can start with the inherent *localized* nature of d-electrons. This is tied with the Hubbard U which further favours localized behaviour and acts as a penalty to charge transport from metal to metal atoms in solids. However, there is a certain degree of itinerant behaviour tied together with orbital overlap and charge hopping when "d-atoms" form compounds and solids. It is the competition of the localized and itinerant behaviour that determines how "correlated" materials are and which theoretical models are appropriate for treating them. Finally, only two fundamental quantities, the charge transfer energy and Hubbard U, can determine much of the characteristics of TMOs.

Chapter 4

X-ray Spectroscopy

X-ray spectroscopy is a very valuable tool for the investigation of the properties and electronic structure of matter. The energies of soft X-rays (about 50 - 2000 eV) make them ideal for excitation of core level electrons in solids allowing the examination of electronic structure. It is the measurement of the excitation and relaxation back into the ground-state that allows the probing of partial occupied and unoccupied electronic states.

X-rays interact with matter in three main ways: they can be transmitted without any interaction with the sample, scattered either elastically (change in momentum but not energy) or inelastically (change in momentum and energy), and absorbed, where the X-ray energy is imparted to the matter. Only the absorption interaction is of interest to this research and will be discussed.

4.1 X-ray Absorption Spectroscopy

When X-rays of energies slightly larger than the binding energy of core electrons in a sample are incident on a sample, the photon energy can be absorbed by a core electron which can be excited to a state above the Fermi level which is normally unoccupied in the ground-state. These previously unoccupied states are called conduction band states. Elements have different and characteristic electron binding energies and by tuning the incident X-ray energy, different elements can be excited and probed; this is what is meant by the term "element specific". The excited electron originated in a particular quantum state (n, ℓ, m, σ) on a particular atomic site, and now occupies a different excited state. The transition is governed by the dipole allowed selection rules which state that angular momentum must be conserved.

Since the incident X-ray (i.e. photon) carries angular momentum $\ell = 1$, the excited electron must be in a state with $\Delta\ell = \pm 1$. This is the origin of the term "*partial/projected* density of states" (pDOS); the XAS measurement gives a measure of the DOS of particular angular momentum. In the case of O $1s$ XAS, the initial state is a $1s$ state with $\ell = 0$, thus the final state must have angular momentum $\ell = 1$, that is, it must be a p state. So O $1s$ XAS probe unoccupied O p-states. The actual measurement of X-ray absorption processes are not of concern here. It is sufficient to understand that the amount of absorption as a function of X-ray energy gives a measure of the pDOS at an energy related to the incident X-ray energy.

4.2 X-ray Emission Spectroscopy

The relaxation back into the ground-state after the excitation of a core electron can occur in several ways. One possible channel is that a valence electron on the excited atom will fill the core-hole. When this occurs a photon is emitted that has an energy equal to the binding energy of the valence electron that filled the hole minus the energy of the hole state. Measurement of these emitted photons gives a measure of the pDOS of occupied valence states. The same selection rules apply to this process as in XAS; thus, O K-edge XES measures occupied O $2p$ states.

4.3 Core-hole Effect

In an XAS measurement the final state being measured consists of a core-hole vacated by the excited electron which is now in a excited state. The measurement is not a measure of the exact ground-state of the system; it is perturbed by the core-hole which effectively reduces the screening of the nuclear charge and causes the unoccupied states on the excited atom to be more tightly bound to the nucleus. This effect can be estimated by introducing a core-hole into a DFT calculation and measuring the difference in the conduction band onset energy of the ground-state calculation (normal DFT calculations) and the core-hole calculation [36]. XES measurements are negligibly affected by the core-hole since the final state being measured includes a hole in the valence band which has a much weaker effect.

Chapter 5

Experimental and Computational Methods

All samples were commercially available powders (Alpha Aesar, 99% purity) mounted on carbon tape with no further processing. The oxygen K-edge XES and 1s XAS measurements were carried out on Beamline 8.0.1 of the Advanced Light Source (ALS) at Lawrence Berkeley National Laboratory. The XES measurements used a Rowland circle geometry X-ray spectrometer with spherical gratings. The oxygen K-edge XES was excited well above resonance at 560 eV. The resolving power of the spectrometer ($E/\Delta E$) was about 1000.

The oxygen 1s XAS was measured in the bulk sensitive total fluorescence yield (TFY) mode. Spectra were normalized to incident photon flux using the photoelectron current from gold mesh upstream of the sample to correct for beam fluctuations. The resolving power or the monochromator for XAS measurements was about 2000. The experimental spectra were energy calibrated by using peaks in the spectra of a well-characterized reference sample, BGO. The calibration standards are in Tables A.1 and A.2 in Appendix A.

The oxygen edges were chosen for the experimental spectra for the following reasons. All samples studied contain oxygen so the method is consistent. The resolution at the oxygen edges is much higher than at the metal L-edges since resolution scales inversely with energy. The relevant Ag edge (L_2 at 3524 eV) is inaccessible to soft X-rays. Furthermore, it has been shown that O $1s$ XAS is not strongly influenced by the core-hole effect while the transition metal $2p$ XAS is strongly effected [35].

All calculations were performed with the WIEN2k code [37]. WIEN2k is a full potential linear augmented plane-wave plus local-orbital (FP-LAPW + lo) code which can handle a wide variety of exchange-correlation functionals.

Crystal structure and symmetry data are entered and the code calculates the corresponding "muffin tin" regions and basis set as follows: the unit cell is divided into spheres surrounding nuclei and interstitial regions between spheres. The "muffin-tin" sphere radius is chosen as to restrict localized core electrons to the nucleus to which they belong, while allowing semi-core and valence electrons to be delocalized [36]. Spherical harmonics times radial functions are used as the basis set inside the spheres while Block plane waves are used in the interstitial region. Boundary conditions are implemented to enforce continuity of the wave functions and derivatives at the intersection of the two regions.

The basis set is evaluated only at certain points in k-space and a grid of K points must be specified. A dense k mesh will increase accuracy but also increase calculation time, so a compromise must be made. Typically a 1000 point k-mesh is a good compromise.

Once a calculation has converged there are several other packages with which to calculate physical properties from the calculated ground-state density. Total and partial DOS for each desired site or symmetry, XES and XAS spectra, magnetic properties, and band structure diagrams can all be calculated. The structural and computational parameters are shown in Table 5.1.

Table 5.1: Structural and calculational parameters.

Compound	Space group	β (°)	a (Å)	b (Å)	c (Å)	Metal site	Oxygen site	k grid, k_a x k_b x k_c	R_{MT}^{metal}	R_{MT}^{O}
CuO[38]	$C2/c$	99.54	4.6827	3.4226	5.1288	4c	4e	12 x 6 x 12	1.9	1.68
AgO[39]	$P2_1/c$	107.54	5.8592	3.4842	5.4995	2a, 2d	4e	8 x 13 x 8	2.0	1.78
Ag_2O[40]	$Pn\bar{3}m$	90	4.7306	4.7306	4.7306	4b	2a	10 x 10 x 10	2.04	1.81
Cu_2O[41]	$Pn\bar{3}m$	90	4.27	4.27	4.27	4b	2a	10 x 10 x 10	1.87	1.61

Theoretical calculations for all samples were done using the following exchange-correlation functionals.

- The generalized gradient approximation of Perdew-Burke-Ernzerhof [42].
- An on site Coulomb potential U added to PBE for the metal d-states (PBE+U). A typical initial value of U=4.0 eV was used for all cases and this is the value used in the comparisons with other functionals. A discussion of the proper U value will follow in chapter 7.
- Hybrid functional based on a ratio of PBE correlation and Fock exchange, labelled Hartree-Fock (HF) [27, 28]. A typical value for the mixing of $\alpha = 0.35$ was used [17].
- Modified Becke-Johnson potential was used to calculate more accurate bandgaps [30].
- An on site Coulomb potential was also added to the MBJ potential (MBJ+U).
- The screened hybrid functional of Heyd, Scuseria, and Ernzerhof which uses a screened Coulomb potential to represent the exact Hartree-Fock exchange is used for Ag_2O and Cu_2O [28].

Core-hole calculations were performed on 2 x 2 x 2 supercell with one oxygen 1s electron removed and a background charge of e^- added to simulate the core-hole due to the O 1s vacancy. Calculations without the core-hole were also done for comparison purposes and to investigate the effects of the core-hole. All X-ray spectra were calculated from the calculated density of states using the XSPEC program in the WIEN2k code. The partial density of states is multiplied by a transition probability matrix to estimate the X-ray spectra. The calculated spectra were broadened with a Voigt function to simulate the Gaussian-shaped experimental resolution and the Lorentzian-shaped life-time broadening of the experimental spectra.

The Fermi energy and bandgaps were estimated by using local maxima in the second derivative of the experimental spectra. The Fermi level is taken as the local maxima on the high energy side of the XES spectra. This method is consistent and has been shown to be very useful for estimating Fermi levels and bandgaps [35]. The calculated DOS and X-ray spectra are aligned with the Fermi level obtained from the second-derivative-method to allow comparison of calculations and experiment.

There is no single quantitative criteria used in the comparison between experiment and calculations; the general shape and features of the spectra are used to determine the best agreement. There are several reasons for this. First, functionals are often developed to prioritize accuracy of one specific property while sacrificing others, introducing an inherent bias. For instance, if the bandgap was used as the comparison criteria, MBJ would likely outperform others. Second, the interesting states in TMOs are typically the bonding states in the valence band; it has been shown that the bonding states (which are naturally lower in energy) are located deeper in the valence band [43]. The most reliable way to probe these states is through XES; X-ray photoelectron spectroscopy (XPS) can probe the valence states, but is very surface sensitive and cannot penetrate into the bulk of a material. Thus, to study the interesting valence band states one needs to clearly distinguish certain bands, their intensity and location (with respect to energy). The best way to do this is to look at the general shape and location of features in the X-ray spectra. The conduction band probed with XAS will be discussed more briefly than the valence band. Information that can be obtained from XAS includes local structural information (bond lengths, coordination environments, etc.) chemical speciation, and electronic structure. The electronic structure information can be derived from the location and intensity of the XAS features; thus, only these aspects will be considered.

Chapter 6

Results

This chapter examines the performance of the different functionals with respect to reproducing experimental results. General features of the calculated X-ray spectra and DOS will be discussed, and conclusions are made as to which functionals perform the best.

6.1 AgO

AgO has important applications in battery technologies [2] and has interesting bacteriostatic properties [5]. It is known to be an n-type semiconductor with a bandgap of about 1.0 eV [44]. It crystallizes in the monoclinic space group structure $P2_1/c$. It has been shown that there are two inequivalent Ag sites with different coordination and valences, Ag(I) and Ag(III) [31] which would make it a $4d^{10}/4d^8$ system with closed d-subshells. The Ag(III) atoms are square planar coordinated with oxygen, while the Ag(I) atoms are linearly coordinated. The unit cell of AgO is shown in Figure 6.1.

Figure 6.2 shows the experimental and calculated X-ray spectra for the different functionals. In general, PBE and MBJ most accurately reproduce the experimental spectra. The calculated XAS look nearly identical, the only outlier is MBJ+U which shows less structure between the main low energy peak at 529.5 eV and the second peak which should be at 537 eV, but is shifted up in energy to about 539 eV. A discussion of the core-hole calculation will follow in section 8 and is included here for completeness. The calculated XES is also quite good, with PBE performing the best. PBE does show more peak splitting, labelled by C, than MBJ; this splitting can be seen in the experimental spectra as well. PBE+U, MBJ+U, and HF all show a distinct shoulder on the low energy side of the main emission peak at

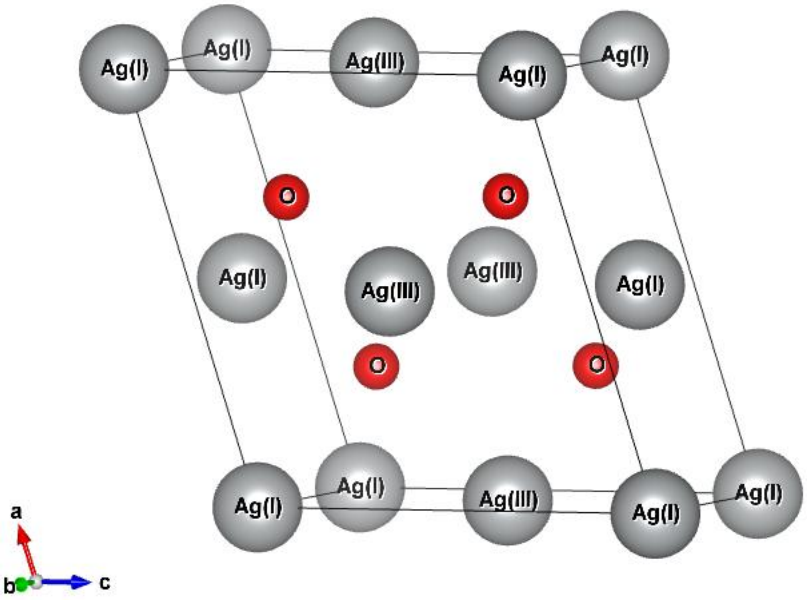

Figure 6.1: The unit cell of AgO showing the different Ag sites.

A. The effect of adding the U term and *localizing* the *d*-electrons is to shift the *d*-states to lower energies; this gives rise to the secondary peak at A. The shoulder on the high side of the main emission peak at B is more pronounced in the +U and HF functionals than it is in the PBE and MBJ. The Fermi energy found from the second derivative (shown in section 8) is at 528.3 eV.

It is interesting that the PBE without the +U gives better results than PBE+U. As mentioned above there are two distinct Ag sites with different oxidation states and coordinations. A previous study has shown that PBE alone cannot predict this correct mixed valence structure, but a +U term of more than 5 eV is needed to predict the proper ground-state structure [45]. This suggests that the oxidation state of Ag has little effect on the O *p* valence states in AgO. This seems to contradict the fact that there is a high degree of hybridization of Ag-*d* and O *p*-states throughout the valence band.

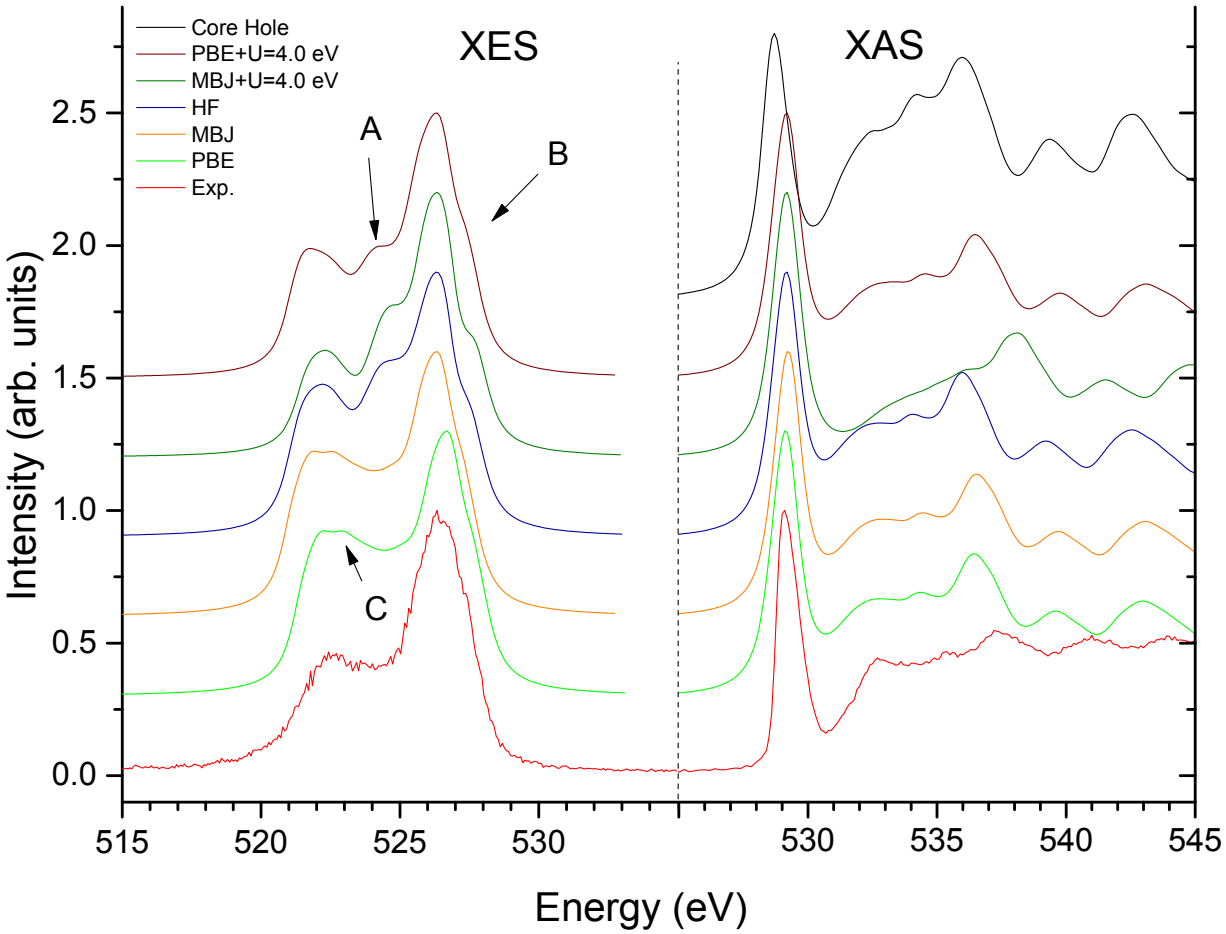

Figure 6.2: Experimental and calculated X-ray spectra of AgO. The energy scale of the XAS has been shifted for clarity, the dotted line represents the split in the energy scale.

The calculated DOS for AgO are shown in Figure 6.3. The symmetry projected Ag *d*- and O *p*-states along with the total DOS are plotted. The Ag *s*, *p* and O *s* DOS are so small in magnitude in the region near the Fermi energy that they are invisible on any meaningful scale and are omitted. The Fermi energy corresponds to 0 eV. The calculated PBE XES is included to facilitate understanding of how spectra are related to DOS.

The PBE and MBJ DOS look nearly identical as expected from the spectra. There are no distinct bands, save for the band between 0 and -1 eV which is distinctly seen in all calculations. There is hybridization of O *p*- and Ag *d*-states throughout the valence band. A

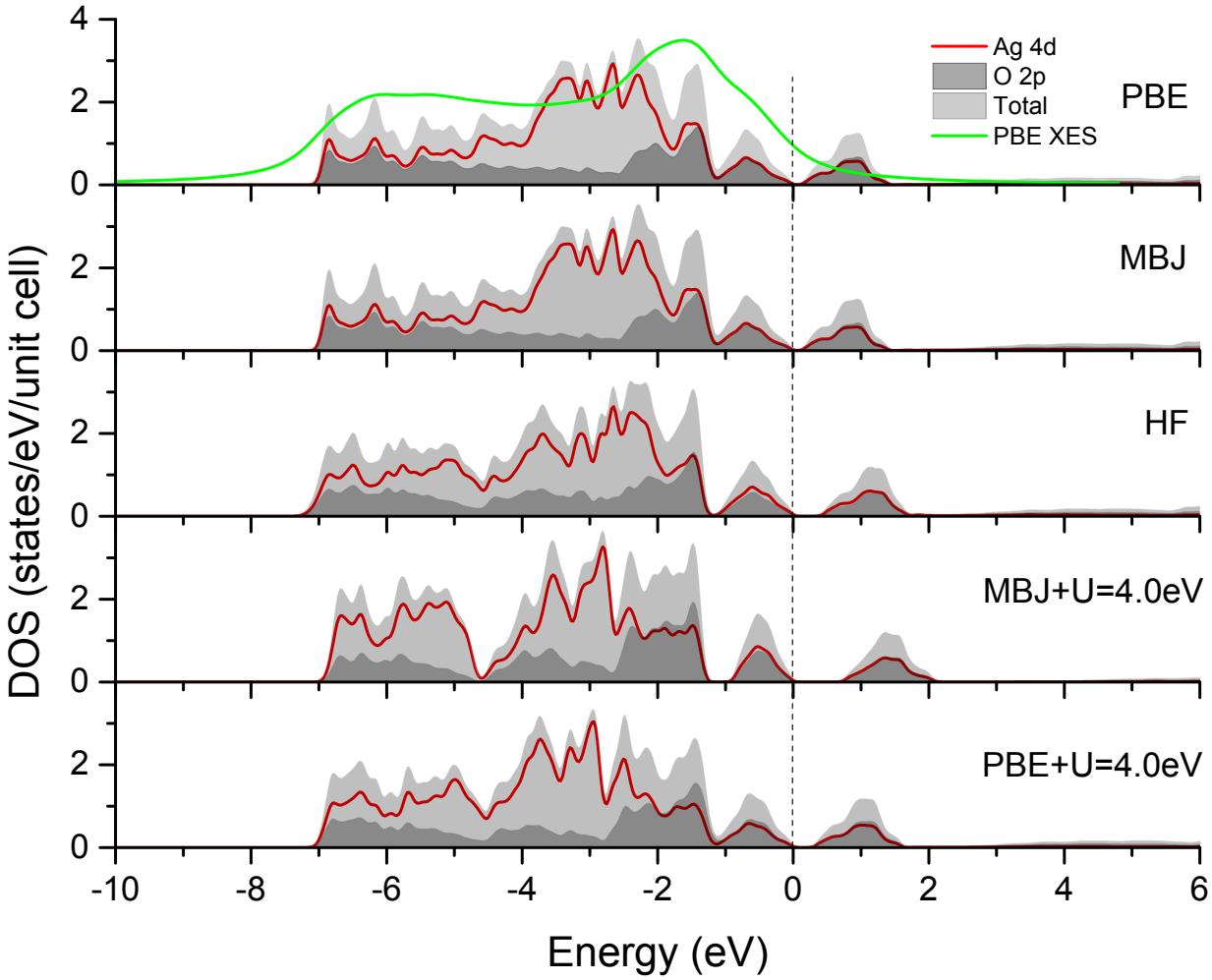

Figure 6.3: Calculated DOS of AgO. The dashed line represents the Fermi energy.

separation of bands at about -4.5 eV starts to form with HF and PBE+U, and is clearly seen with MBJ+U. At first glance, there would seem to be an interesting relationship between the energy location of this band splitting and the value of the U term added; however, the correspondence of the 4.0 eV U-term added to PBE+U and MBJ+U to this band separation at -4.5 eV is not as substantial as it may seem. In the discussion of the +U in chapter 7 we will see that the energy location of the band splitting is not linearly related to the U value added.

Another point of interest in Figure 6.3 is the effect of broadening the calculated spectra. The O p DOS has zero magnitude at the Fermi energy, but the spectrum is not zero. The spectrum does not reach zero until 2 – 3 eV above the Fermi level. The effect of broadening

can also be seen at the bottom of the valence band near -7 eV. However, the calculated and experimental spectra show very similar slopes in their decline after the main emission peak, thus, the broadening applied to the calculated spectra is quite accurate.

6.2 CuO

CuO crystallizes in the monoclinic space group C 2/c with an open d-shell ($3d^9$); the unit cell is shown in Figure 6.4. It is an antiferromagnetic semiconductor with a bandgap between 1.4 – 1.9 eV, depending on sample preparation methods [41, 46]. CuO has applications in battery technology and the basic structural unit is similar to the Cu_2O layers in high temperature superconductors and is, therefore, of great interest [41]. Ghijsen et al. have determined the Cu *d*-*d* and O *p*-*p* Coulomb interactions, the O to Cu charge transfer energy, and the degree of Cu-*d* to O-*p* hybridization and determined that CuO is a charge-transfer insulator in the Zaanen, Sawatzky, and Allen model [34].

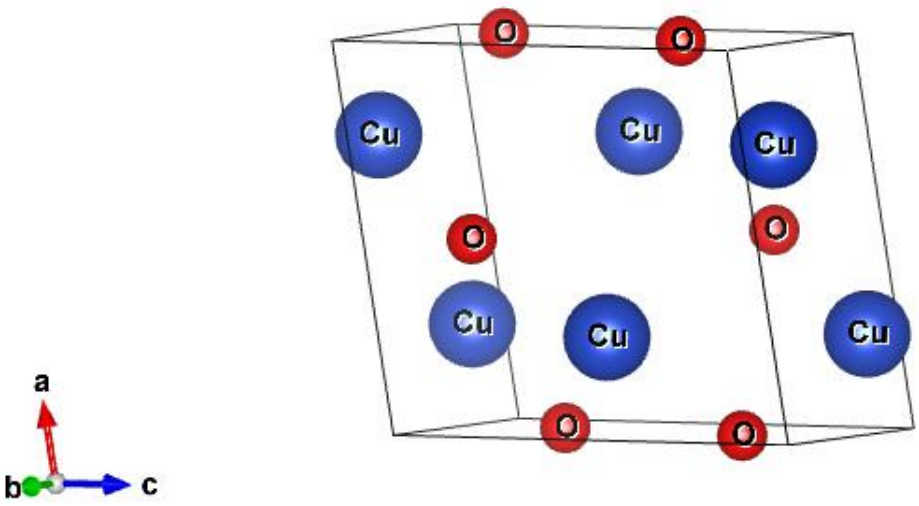

Figure 6.4: Unit cell of CuO.

The nature of the XAS and XES spectra makes it necessary to plot them separately to be viewed coherently. The XAS are shown in Figure 6.5.

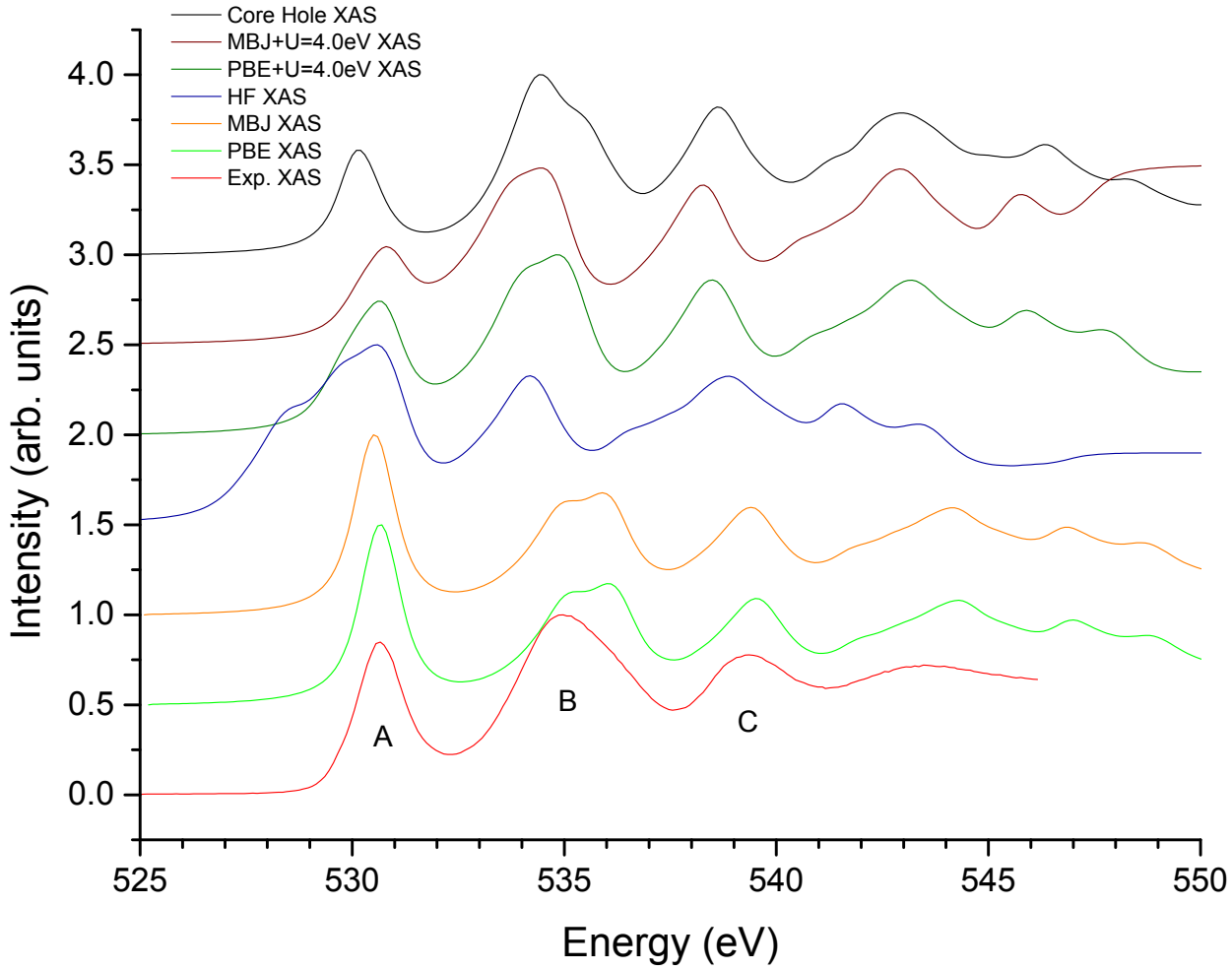

Figure 6.5: Experimental and calculated XAS spectra of CuO.

The important features in the XAS spectra are the location and relative intensities of the three main peaks labelled A, B, and C. PBE, MBJ, and HF incorrectly have peak A as the most intense and have the location of peak B at the wrong energy. HF also incorrectly shows a large shoulder on the low energy side of peak A. The PBE+U calculation correctly locates the three peaks and has the peak intensities that most closely match experiment.

Figure 6.6 shows the XES spectra of CuO; the Fermi level is at 529.8 eV. The experimental spectra shows very even peak intensities of peaks A and B at 524.5 and 526.5 eV,

respectively. This spectrum is nearly identical to that measured by Mariot et al. [47]. None of the functionals get the peak ratios correct and all show more secondary peaks that are not present in the experimental spectrum. It appears that the +U functionals come closest to the correct ratios and it will be shown in chapter 7 that indeed a +U term is needed to predict the proper peak ratios for CuO. Mariot et al. have attributed the discrepancy between experiment and DFT calculations (with respect to the peak ratios and locations) to extra correlation effects as a consequence of the open $3d^9$ configuration of Cu(II). [47].

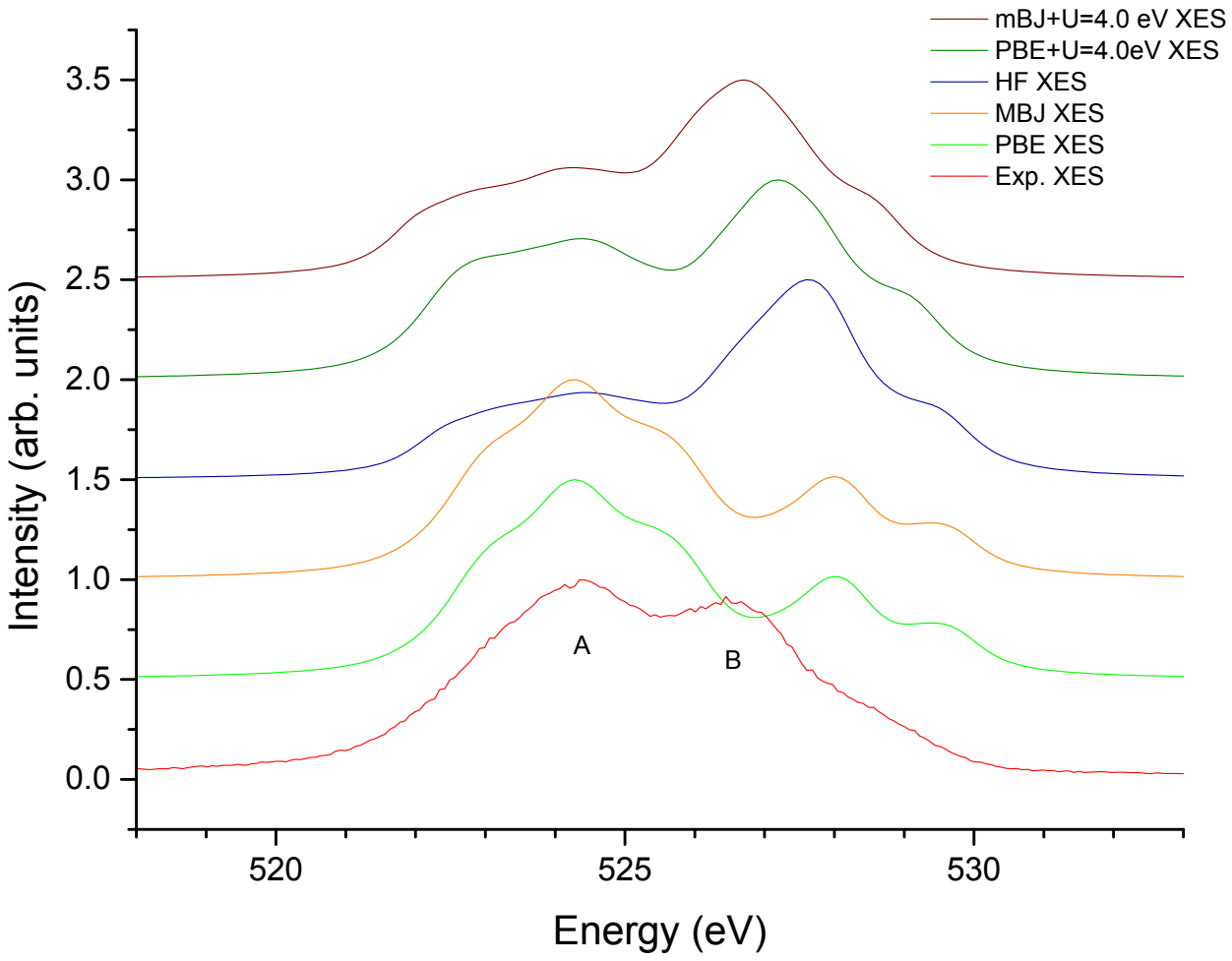

Figure 6.6: Experimental and calculated XES of CuO.

The DOS for CuO are shown in Figure 6.7. The most obvious point is that we see the effects of localizing the *d*-states. The +U schemes and HF method all have the *d*-states at lower energies. The crude interpretation of the effect of adding a Hubbard U term is

to literally increase the attractive potential between the host nuclei and the d-electrons, increasing the binding energy and shifting the d-states lower in energy. A correlated feature to this is the shift in intensity of the O p-states. There are two fairly distinct O p-bands, separated at about -3 eV in the PBE and MBJ, and at about -4 eV in the +U and HF calculations. As the d-states shift lower in energy in the later schemes, the O p-states are shifted higher in energy, increasing the intensity of the higher energy band; this leads to the change in peak ratios that is seen in the spectra in Figure 6.6.

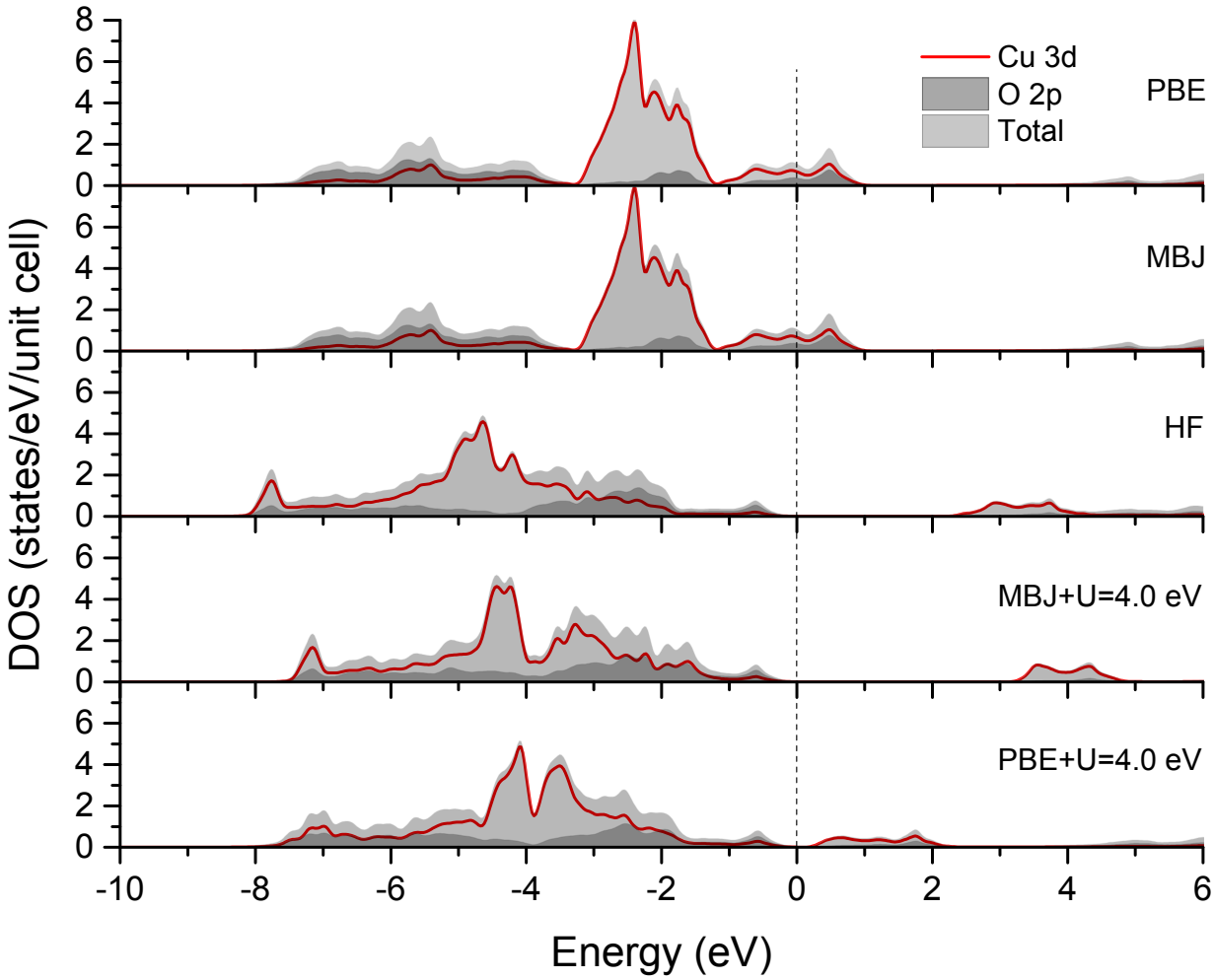

Figure 6.7: Calculated DOS of CuO. The dashed line represents the Fermi energy.

Ghijsen et al. have classified CuO as a strongly correlated system with a very large degree of Cu d - O p hybridization [47]. The degree of hybridization between anion and cation can be in general seen by the location of the d-states; the greater the hybridization,

the lower the d-states will be [48]. The shift of d-states to lower energy in the +U and HF schemes suggests a higher degree of hybridization. We also observe strong hybridization in the conduction band. This is somewhat surprising since there are few unoccupied Cu d-states available to mix with O p-states. Furthermore, metal d-orbitals shrink in later TMOs making hybridization less probable. The fact that a +U term is needed to properly reproduce the experimental spectra agrees with their classification of a strongly correlated system.

6.3 Ag_2O

Ag_2O crystallizes in the same cuprite structure as Cu_2O, space group Pn-3m. The unit cell is shown in Figure 6.8. The Ag atoms are linearly coordinated with O atoms, as expected in a closed d^{10} system, and the oxygen are tetrahedrally coordinated with Ag. However, the idea of simple ionic bonding of Ag^+ (with a d^{10} configuration) with O^{2-} has been challenged. Difference electron density mapping has shown that there is hybridization between metal and oxygen atoms that brings about a charge transfer from metal to oxygen atoms, and also an intraatomic transition in the metal $d^{10}s^1 \longrightarrow d^9s^1$ [48, 49]. Such a configuration would make Ag_2O and Cu_2O unfilled d-systems with characteristics more similar to CuO than AgO.

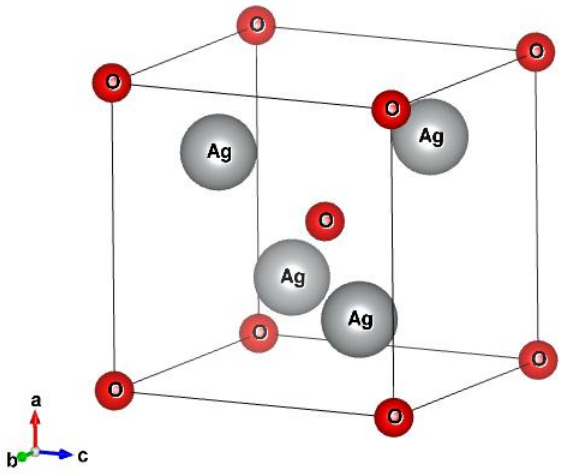

Figure 6.8: The unit cell of Ag_2O.

The spectra for Ag_2O are shown in Figure 6.9. The XAS spectra all look very similar. The core-hole calculation does show a little more structure in the region between the two main peaks, but the rest of the calculations are nearly identical to each other and in good agreement with experiment.

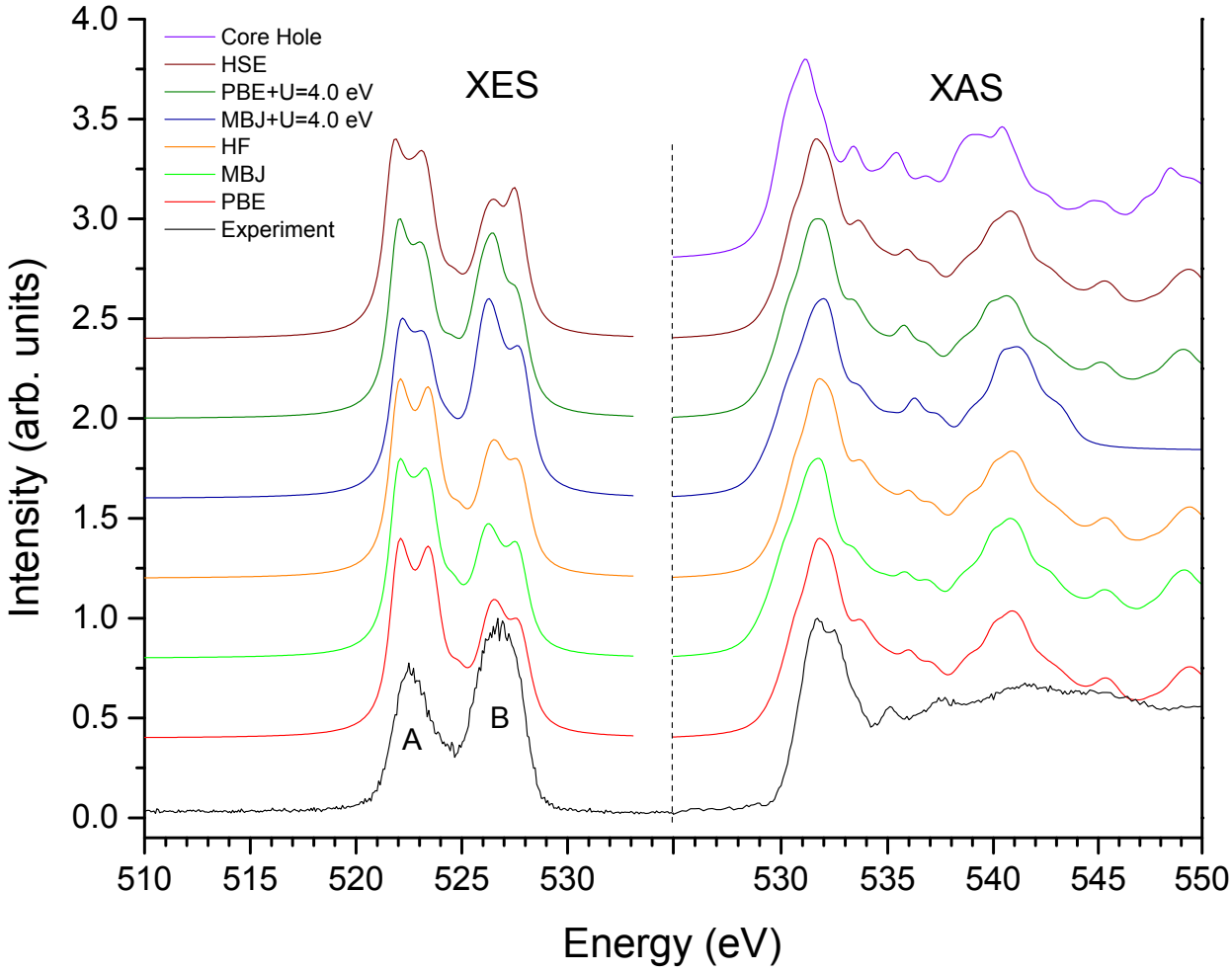

Figure 6.9: Experimental and calculated X-ray spectra of Ag_2O. The energy scale of the XAS (right) has been shifted for clarity, the dotted line represents the split in the energy scale.

The most obvious feature in the XES spectra is that every functional fails to predict the proper peak ratio of the two peaks A and B. Experimentally, peak B is dominant, but all calculations, save MBJ+U, predict peak A more intense. PBE+U shows almost equal intensity of the two peaks and MBJ+U shows peak B slightly more intense than A. Also, all calculations show a large amount of peak splitting of both peaks in the XES which is not

present in the experiment. It is possible that these peaks should exist in the experimental spectra but are simply not resolved due to broadening effects. Unfortunately, there are no known XES spectra published for pure Ag_2O for comparison. It turns out that tuning the U value in PBE+U will correct the peak ratio and limit the peak splitting. The Fermi energy is 528.6 eV.

The DOS of Ag_2O is shown in Figure 6.10. There are clearly two distinct O p-bands that are separated by a band of Ag d-character that is almost void of any O p hybridization. The O p-bands are, however, strongly hybridized with Ag d-states. The O bands look very similar for all functionals as expected from the similar XES spectra. The presence of two distinct O p-bands separated by a metal d-band is similar to what we see in the calculations for CuO. This is evidence for the unfilled d-shell configuration of Ag_2O discussed above. It will be shown in chapter 7 that the location of the Ag d-states strongly affects the O p-states.

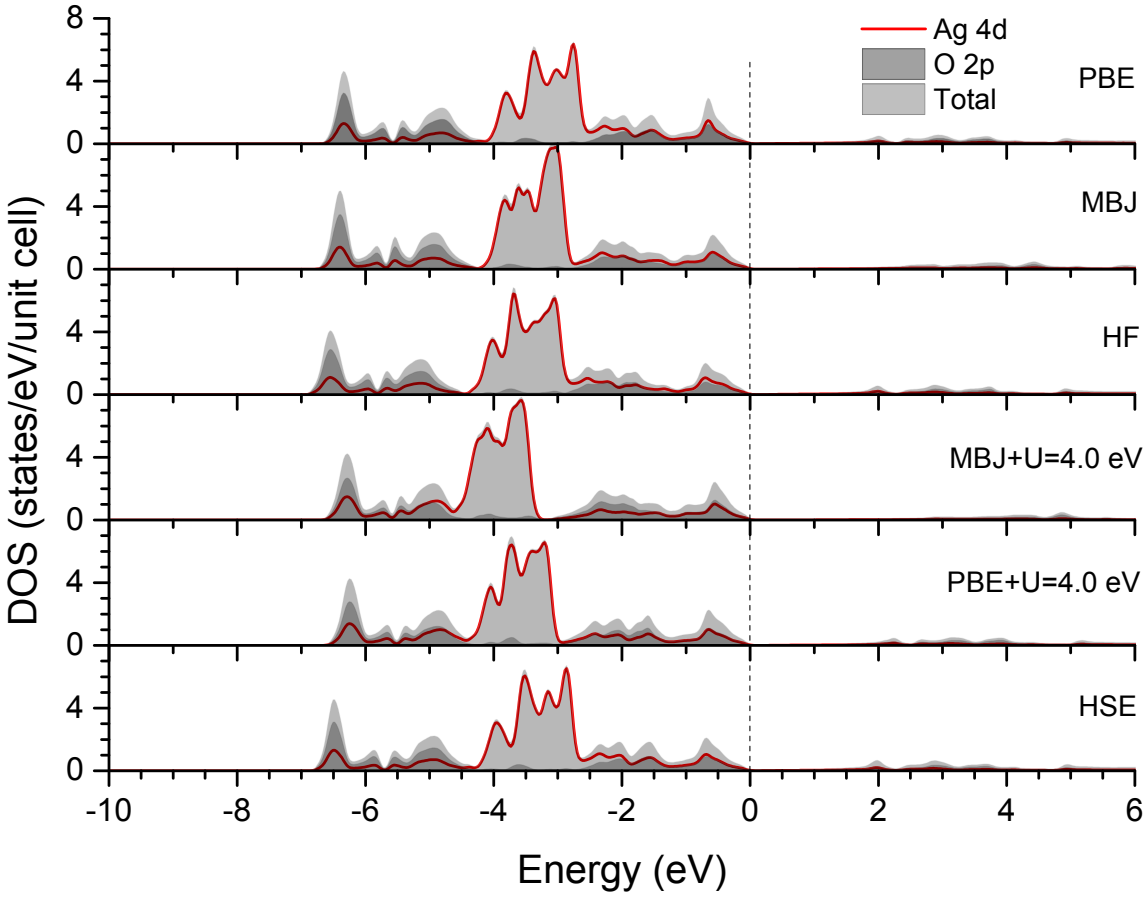

Figure 6.10: Calculated DOS of Ag_2O. The dashed line represents the Fermi energy.

6.4 Cu_2O

Cu_2O shares the same space group as Ag_2O and is a 2.2 – 2.4 eV semiconductor [50, 41]. It has been extensively studied to determine the role of this compound in the generation of high-temperature superconductivity [51]. It has a slightly smaller unit cell due to the less diffuse nature of the Cu *d*-orbitals compared to the Ag *d*-orbitals, but the coordination of the Cu atoms are the same as that of Ag atoms in Ag_2O. It is an open *d*-shell system due to the intraatomic transition discussed above. The unit cell is shown in Figure 6.11.

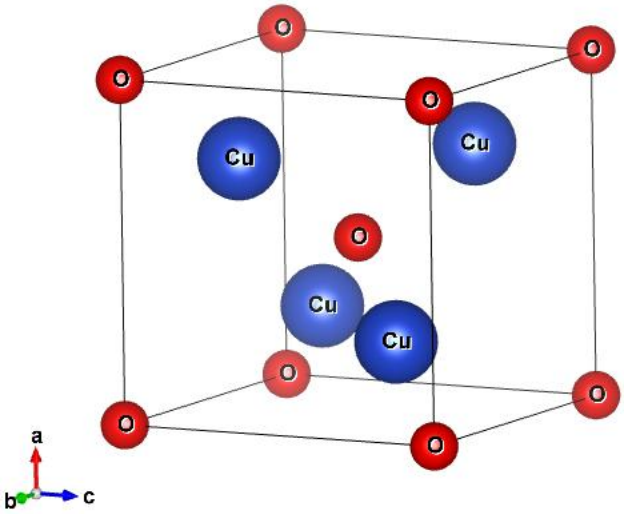

Figure 6.11: The unit cell of Cu_2O.

The calculated and experimental spectra are shown in Figure 6.12. The XAS spectra all look nearly identical save for the core-hole calculation. All calculations reproduce the experimental spectra well.

The XES all show good agreement with respect to the intensity ratio of peaks A and B. There is varying degree of peak splitting of both peaks, however, there is no resolved splitting in the experimental spectra. HSE shows the least splitting and HF shows the most, especially of peak B. The location of peak B does vary somewhat; PBE and MBJ have it at

higher energy than experiment, and the +U and HSE methods place it at approximately the correct energy. The level of splitting does change as the U value is changed as discussed in chapter 7. The Fermi level is at 530.3 eV.

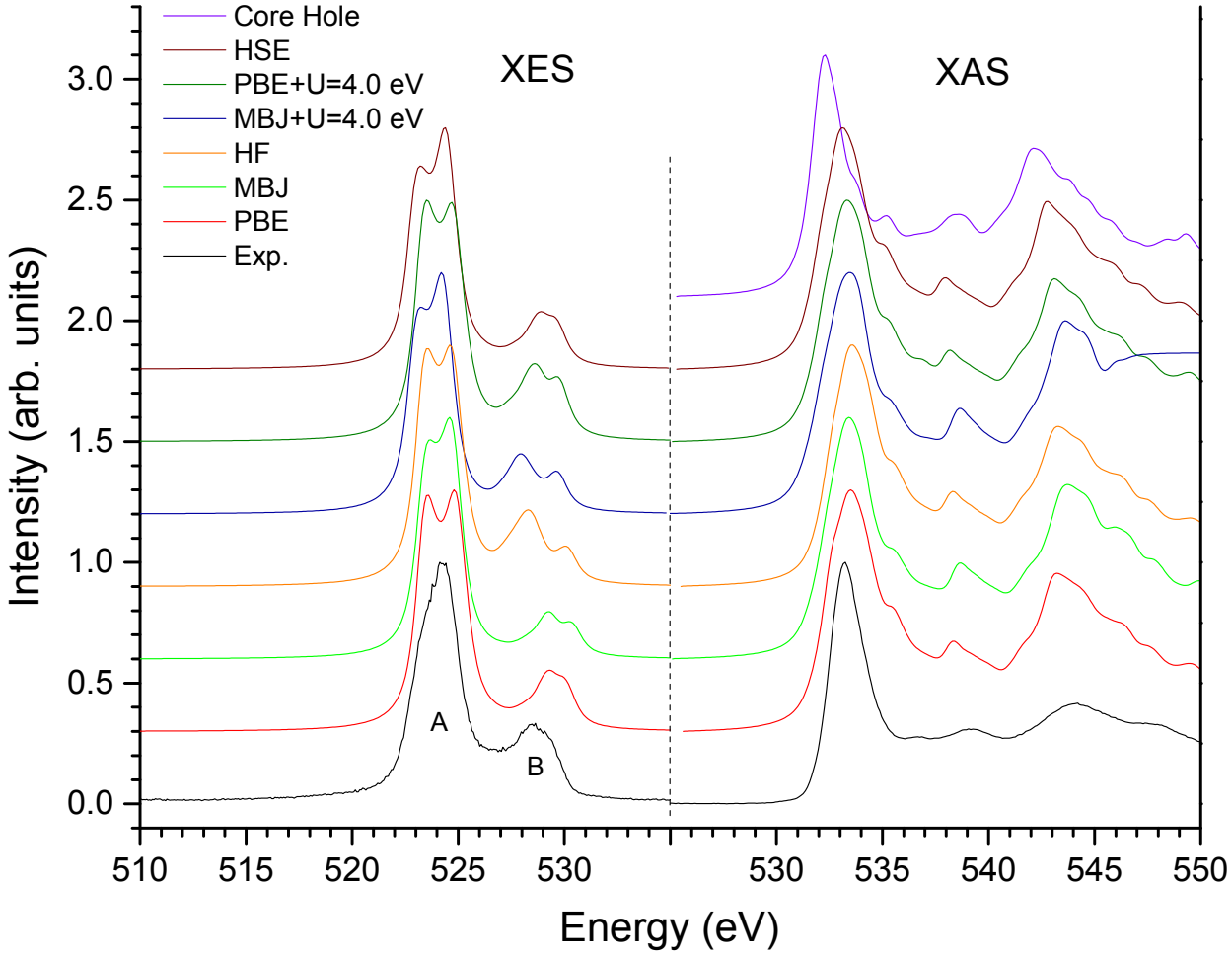

Figure 6.12: Experimental and calculated X-ray spectra of Cu_2O. The energy scale of the XAS (right) has been shifted for clarity, the dotted line represents the split in the energy scale.

The calculated DOS for Cu_2O are shown in Figure 6.13. It is instructive to discuss the similarities and differences between Cu_2O and Ag_2O being that they are isostructural compounds. Cu_2O shows one main O *p*-band between about -7.5 and -5 eV, and a small band just below the Fermi energy that are partially separated by a Cu *d*-band. Ag_2O has the same "two O *p*-band" structure but with a more intense band just below the Fermi level. There is much less metal *d*-character in the O *p*-bands of Cu_2O than Ag_2O. This suggests

more p-d hybridization in Ag_2O, possibly explained simply by the more diffuse Ag d-orbitals that more readily mix with O p-orbitals. The metal d-band is at lower energy in Ag_2O than Cu_2O which is consistent with the premise that greater hybridization shifts this band to lower energy [48].

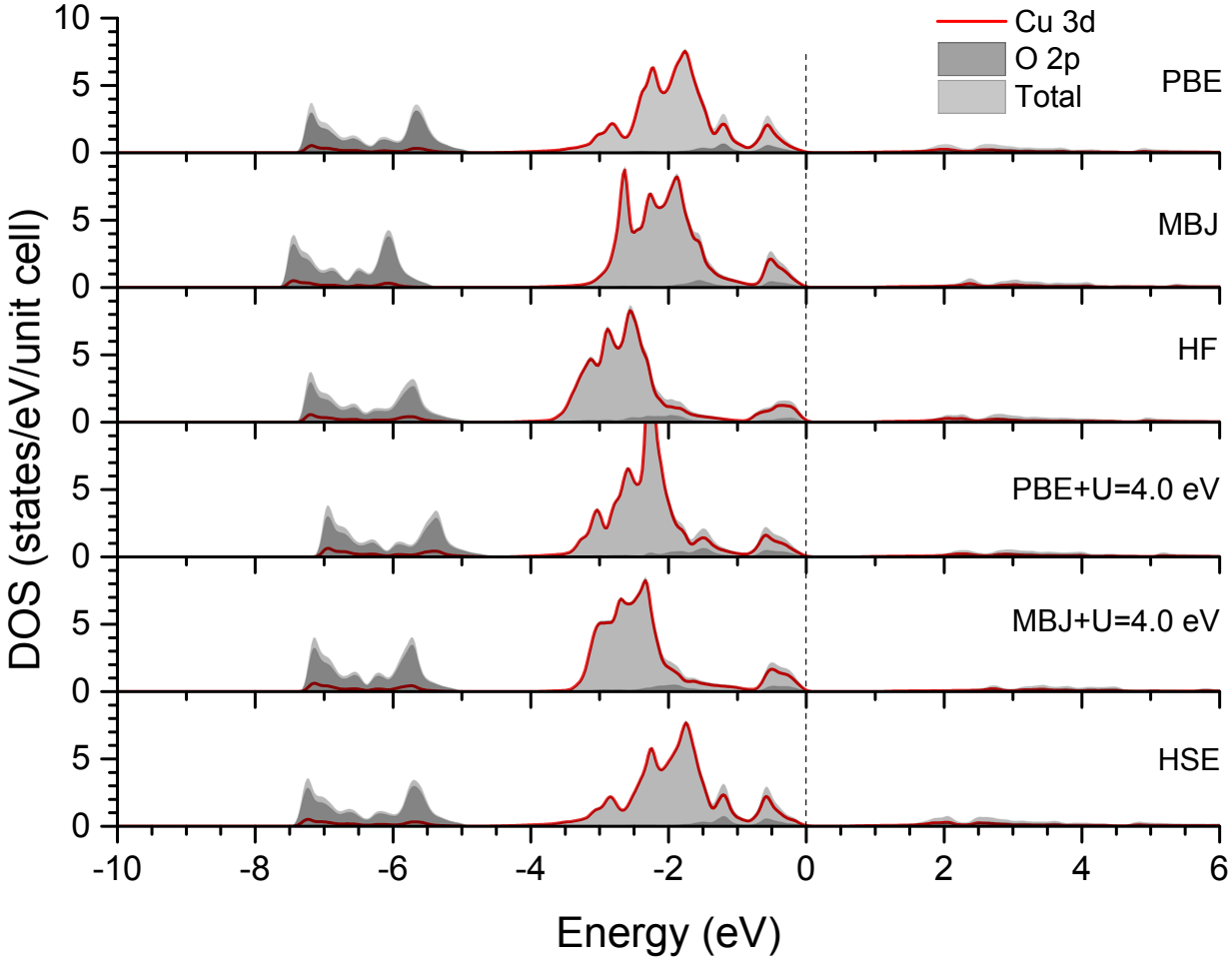

Figure 6.13: Calculated DOS for Cu_2O. The dashed line represents the Fermi energy.

Chapter 7

The Hubbard U Term

7.1 Origin and Implementation

We have seen the origins of the Hubbard +U term in section 3.3; it is an on-site Coulomb repulsion term between electrons of the same orbital angular momentum quantum number on the same atomic site. It acts as an energy penalty to electrons moving through the crystal lattice from site to site. In a standard LDA or PBE DFT calculation the electrons are treated as single particles moving in an "averaged" potential independent of their orbital angular momentum. That is, the potential is orbital independent. The purpose of adding the +U term to the d-electrons is to localize them to their host atom as they inherently should be as discussed in section 3.1. It makes the PBE functional orbitally dependent; the s and p valence electrons are treated with the standard PBE functional while the d-electrons have the added U to their functional. The seminal work on DFT+U was done by Anisimov et al. [52, 25].

The general form of the total energy functional can be written as

$$E^{PBE+U}[\rho, n_{I,\ell,m,\sigma}] = E^{PBE}[\rho] + E^{U}[n_{I,\ell,m,\sigma}] - E^{dc}[n_{I,\ell,\sigma}] \tag{7.1.1}$$

The first term on the right is the total PBE energy based on the total electron density of the system (ρ), the second term is the on-site +U term added to electrons with density n on atomic site I with angular momentum number ℓ, magnetic number m and spin σ. The final term is the double counting correction which corrects for contributions to the total energy that are included in both E^{PBE} and E^{U} [53]. The actual form of the E^{U} term is a topic on its own and will be discussed briefly here. Combining the double counting term and the

Coulomb term, the energy functional can be reduced to

$$E^{PBE+U} = E^{PBE} + \sum_{I,\ell,m,\sigma} \frac{(U_{I\ell} - J_{I\ell})}{2}(n_{I\ell m\sigma} - n^2_{I\ell m\sigma}) \tag{7.1.2}$$

The two terms of interest are $U_{I\ell}$ which is the Coulomb repulsion, and $J_{I\ell}$ which is the exchange energy between electrons with angular momentum ℓ on the same atom I. $n_{I\ell m\sigma}$ are the occupation numbers of states $I\ell m\sigma$ and have values lying between 0 and 1. In practice, the terms are combined into an effective energy

$$U_{EFF} = U_{I\ell} - J_{I\ell} \tag{7.1.3}$$

The U values used in this dissertation are actually the U_{EFF}. The +U term is added to the metal sites (I) with $\ell = 2$ (d-states). All other electrons are treated with the standard PBE functional.

7.2 X-ray Emission Spectra

The results in chapter 6 show that all compounds with the possible exception of AgO benefit from a +U calculation in order to reproduce the experimental spectra. It is the changing of peak ratios, especially in CuO and Ag_2O when adding a +U term, that motivates the investigation of the effects of the U value.

PBE+U calculations with U varying from 1.4 – 16.3 eV were performed on all compounds. The U values were in 0.1 Ry increments for easy implementation in calculations, so the eV values are not round numbers as is often seen in the literature. The calculated XES for all compounds are shown below. Not every U value calculation is shown for reasons of viewing clarity; the important values and enough others to show the trend are shown. The meaning of the vertical dashed line will become apparent in the following sections.

With the spectra not offset vertically we can see in Figure 7.1 that for AgO the PBE calculation (U=0 eV) does indeed have an incorrect peak ratio, with the low energy peak being too intense. The effect of increasing the U value is to lower this peak relative to the

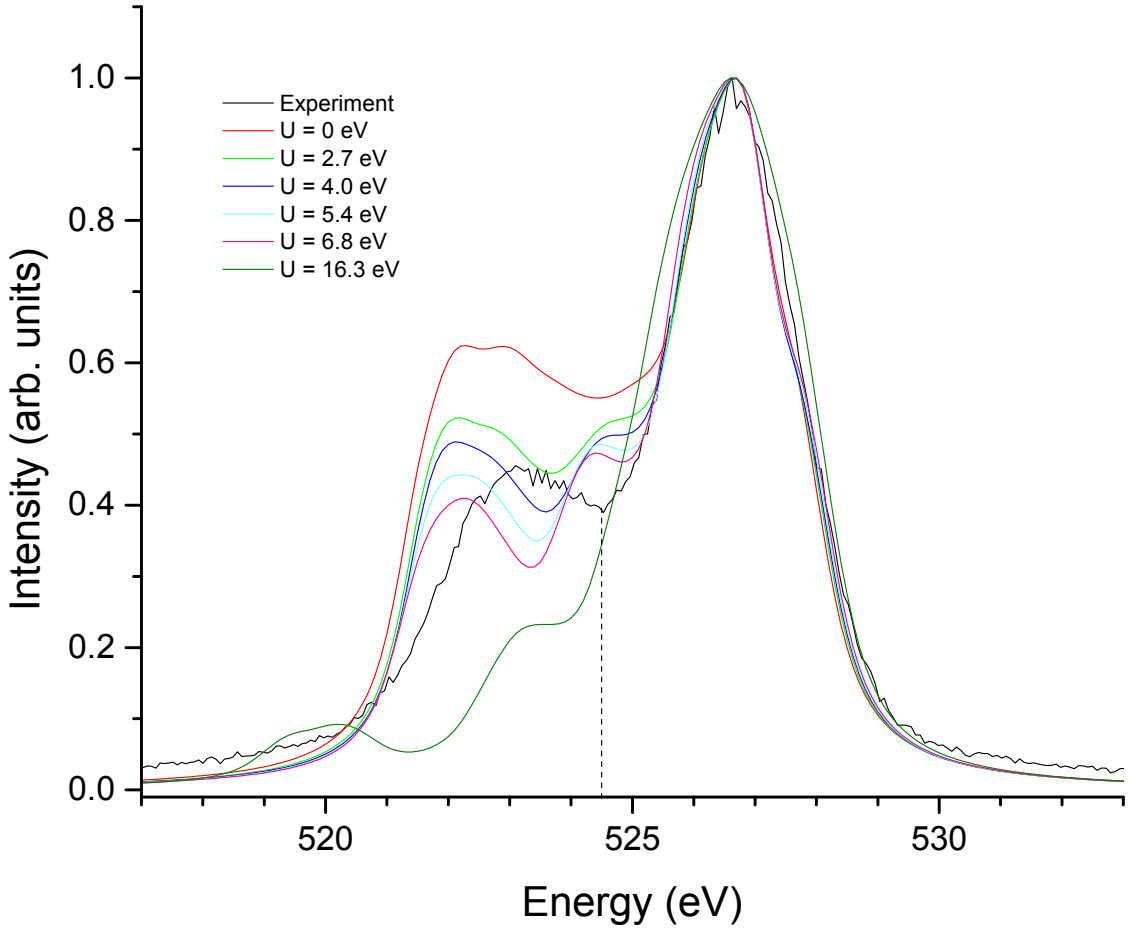

Figure 7.1: PBE+U XES Calculations of AgO.

main peak. The appropriate value seems to be between about 4.0 and 5.5 eV. These values would agree with the result of a U value of at least 5.0 eV needed for AgO from Allen et al. [45].

For CuO we see in Figure 7.2 that increasing U raises the high energy secondary peak in intensity and shifts it lower in energy. The appropriate value is about 2.0 eV. Increasing U past 2.0 eV lowers the main peak incorrectly. This value is much lower than the *ab initio* value calculated by Anisimov et al. of 7.5 eV for copper oxide systems [52].

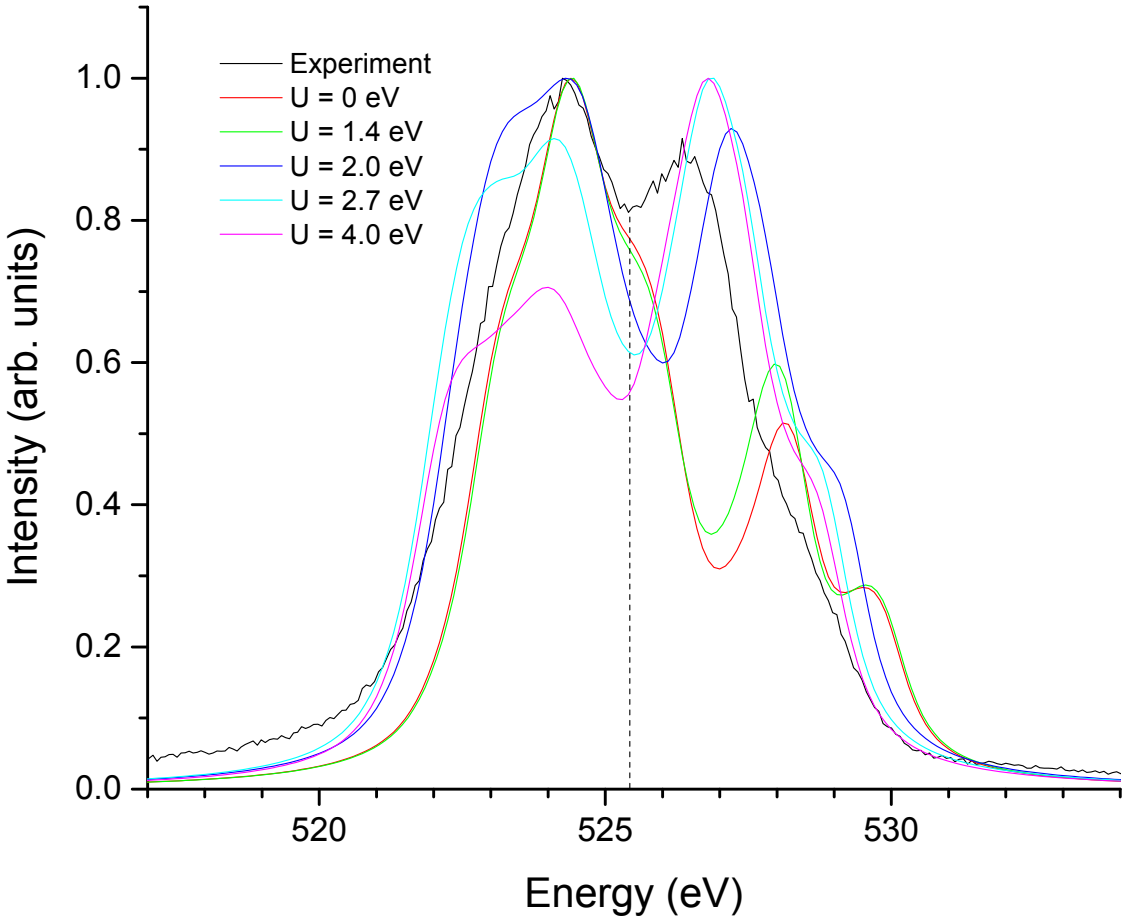

Figure 7.2: PBE+U XES Calculations of CuO.

Adding and increasing the U value for Ag_2O in Figure 7.3 corrects the peak ratio problem from Figure 6.9. The increasing value shifts intensity from the high energy peak to the low energy peak; the optimal value is about 9.5 eV.

Peak ratio optimization for Cu_2O is achieved with a value approximately 4.0 – 5.5 eV as shown in Figure 7.4. There is splitting of the main peak that exists for all values except 6.8 eV; however, this value has the secondary peak too low in intensity.

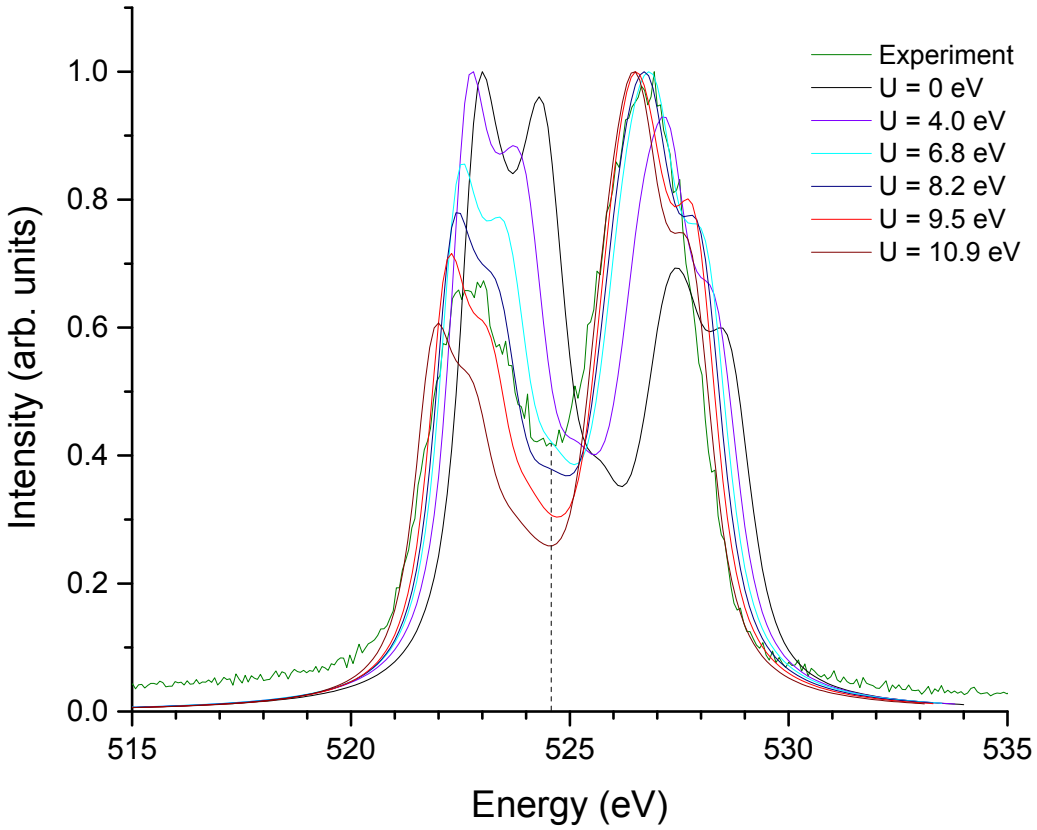

Figure 7.3: PBE+U XES Calculations of Ag_2O.

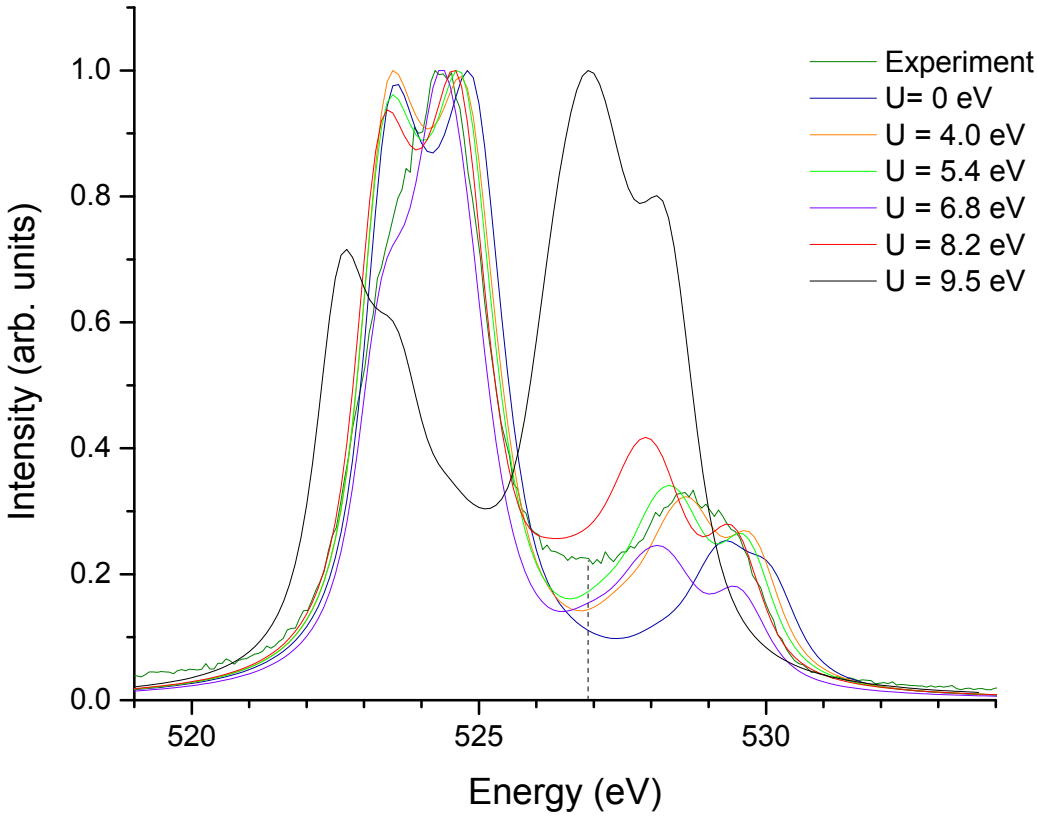

Figure 7.4: PBE+U XES Calculations of Cu_2O.

The general trend of increasing the U value in calculations is to increase the intensity in the high energy peak and decrease intensity of the low energy peak in all compounds. We see that all compounds do indeed benefit from adding a U term to the energy functional. The spectra give an idea of what is happening to the O states in these TMOs; in order to see the correlation with the TM *d*-states we must look at the DOS.

7.3 DOS

The DOS of the various PBE+U calculations are shown below for all compounds. The meaning of the dotted vertical line in the figures will become apparent in the following sections.

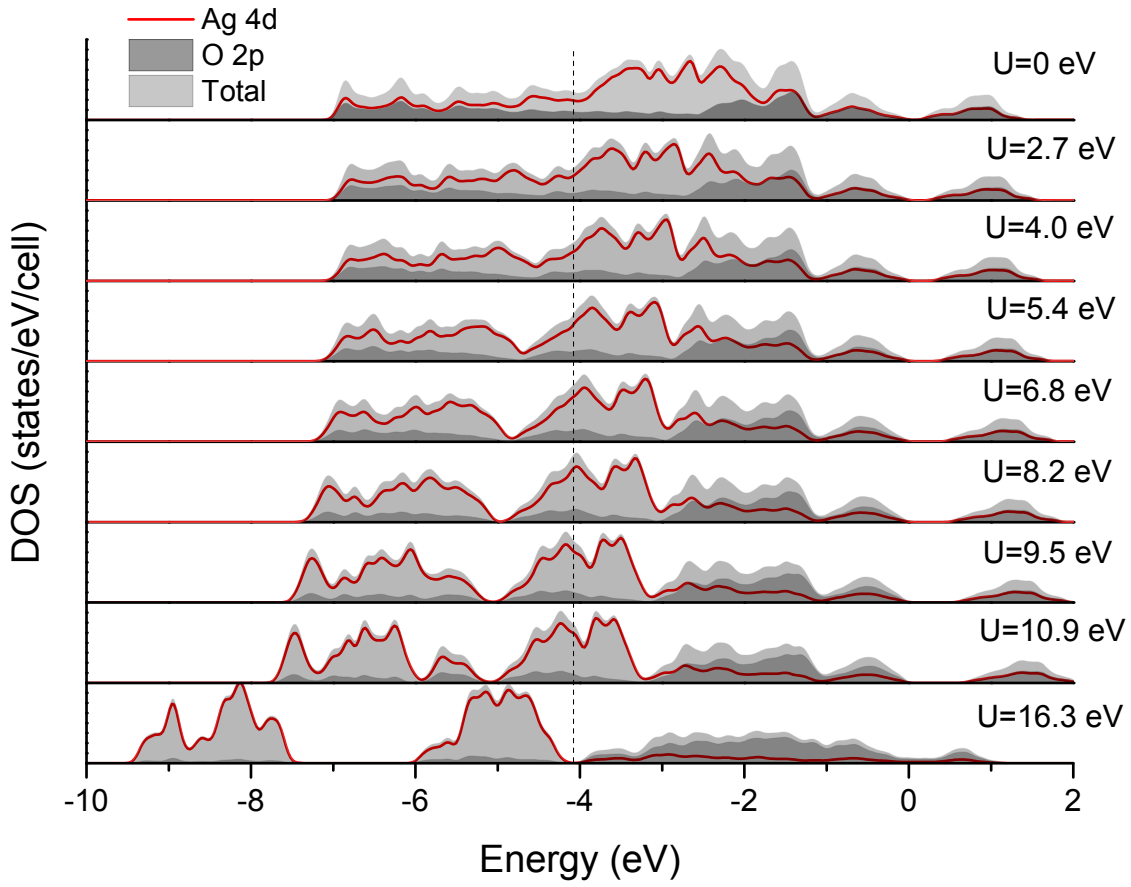

Figure 7.5: Calculated PBE+U DOS for AgO.

In Figure 7.5 the DOS of AgO show the expected trend of the Ag *d*-states shifting lower in energy as the +U term confines them closer to the nucleus. As this happens the O *p*-states that had occupied the energy region now occupied by the shifted Ag *d*-states decrease in intensity; these O states appear at higher energy but do not simply shift up the same way the Ag *d*-states shift down. At very high (non-physically high) U value, the *d*- and O *p*-states become almost completely separate bands with very little hybridization.

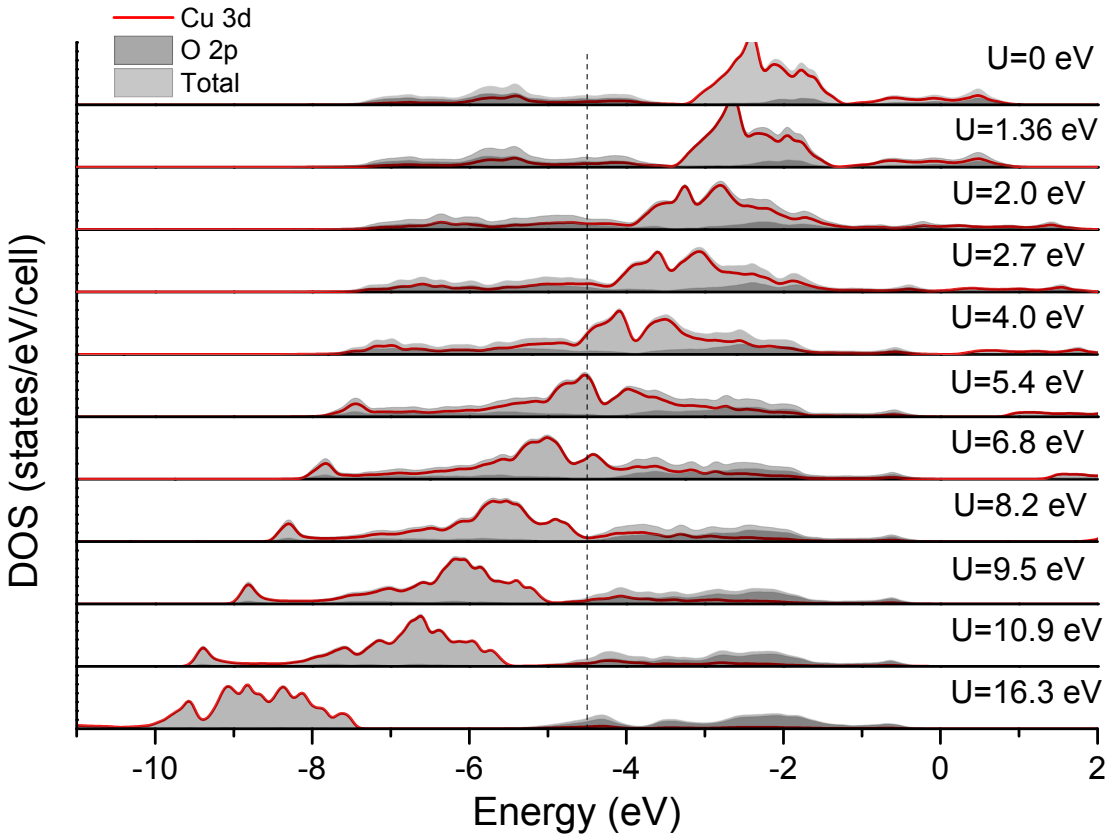

Figure 7.6: Calculated PBE+U DOS for CuO.

The CuO DOS in Figure 7.6 show the same trend as AgO. The *d*-states shift lower in energy and O states move up, with the two bands becoming distinct at high U.

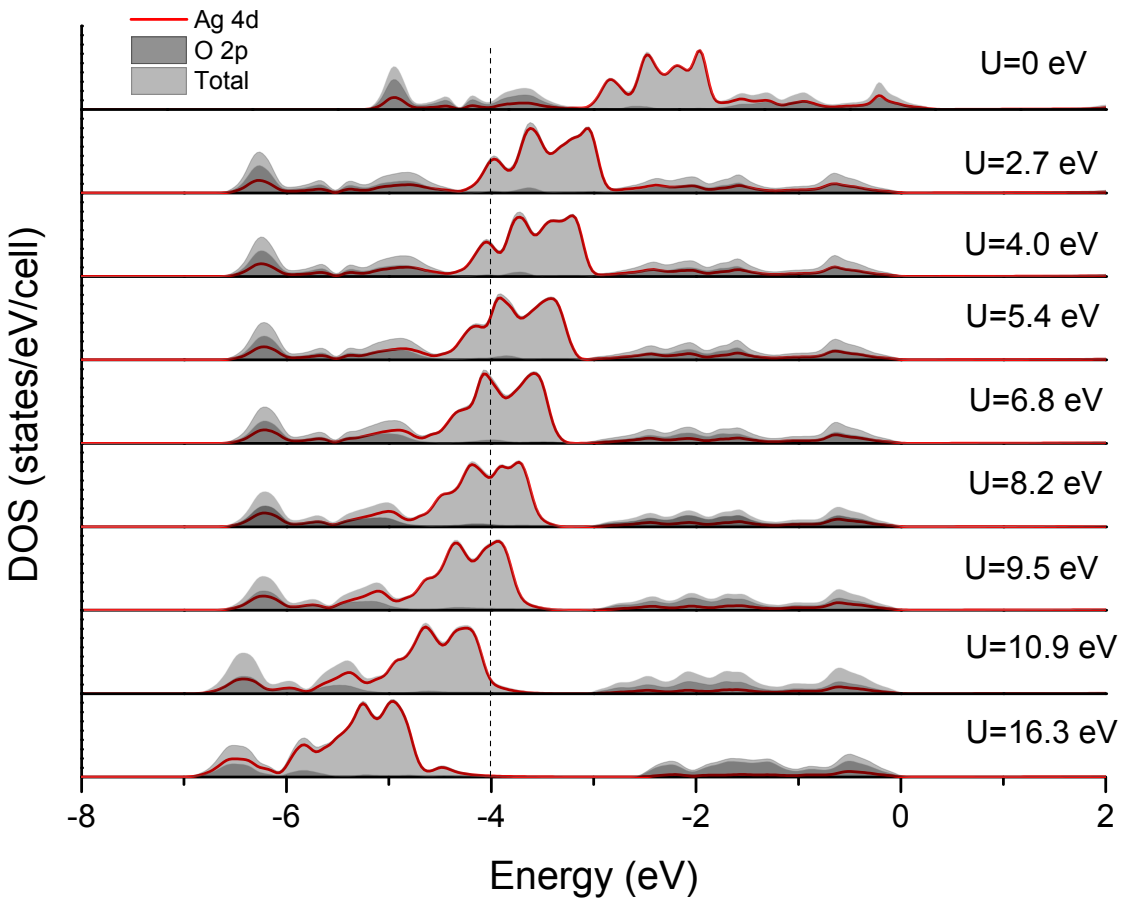

Figure 7.7: Calculated PBE+U DOS for Ag_2O.

Ag_2O in Figure 7.7 displays the same trends as in AgO and CuO. The only difference is that even at high U there is still some O *p*-character at low energy, around -6 eV.

The Cu_2O DOS shown in Figure 7.8 react differently to the U value than the other three compounds. The metal *d*-states do shift down in energy as in the other compounds, however, the difference is the behaviour of the O *p*-states. In Cu_2O the O band on the low energy side of the *d*-states does not decrease in magnitude; it shifts higher in energy as U increases but does not decrease in magnitude. There is a little bit of Cu *d*-character in this O band as well; these *d*-states shift up in energy along with the O states. Also, the O band on the high energy side does not increase nearly as much as in the other compounds.

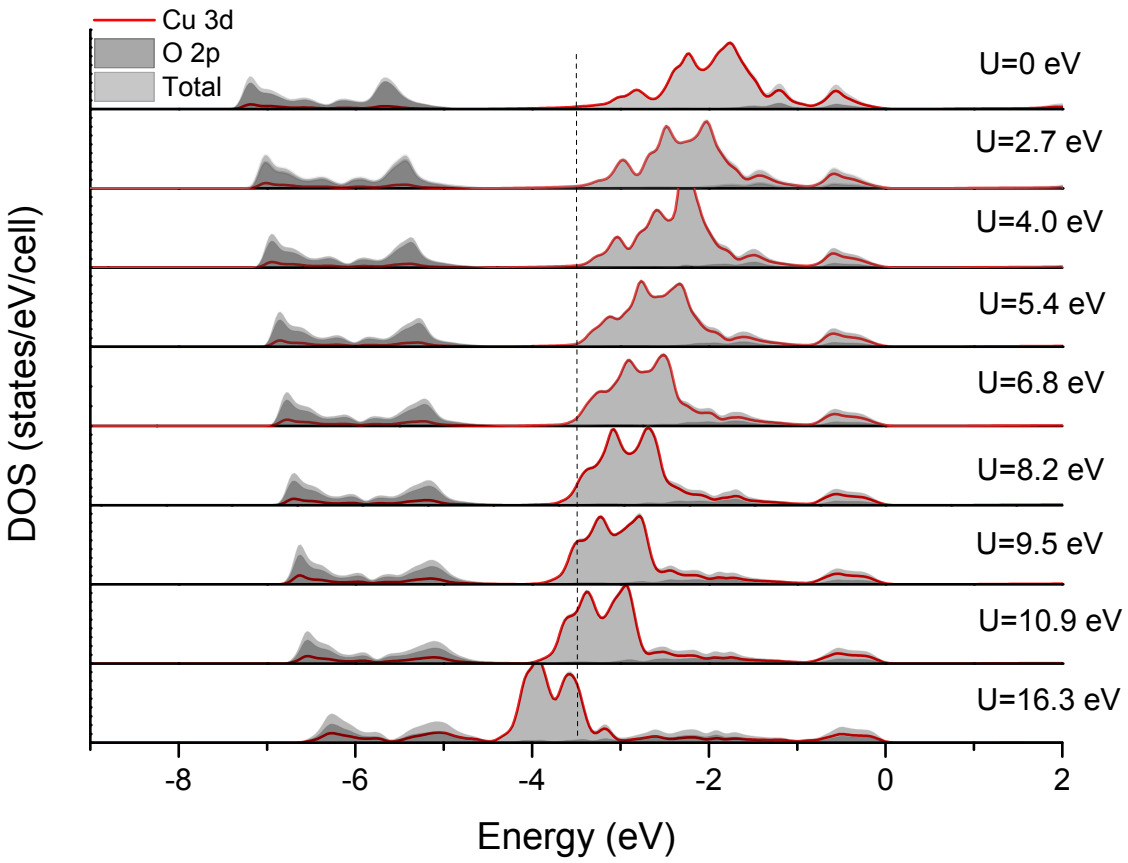

Figure 7.8: Calculated PBE+U DOS for Cu_2O.

It is clear that there is some correlation between the behaviour of the TM d and O p-states in response to the U value. An attempt is made to quantify the correlation and to create a metric with which to predict the appropriate U value for similar TMOs based on experimental X-ray spectra.

7.4 Quantifying the Effects of U

The peak ratios in the oxygen XES of all compounds change when the U value is varied. The +U term is only applied to the TM d-states in the PBE+U calculation, thus, the altering of the O p-states (changing of the XES) is a result of the altered TM d-states. The valence band is separated into two regions in order to compare the response of the TM d and O p-states to the U value. The regions are based on the energy location between the two peaks in the XES. For instance, the location is at 525.4 eV for CuO. This is where the two peaks

are separated as shown by the dashed line in Figure 7.2. The two regions of the experimental XES, referred to as "left" (low energy side) and "right" (high energy side), are integrated to give a measure of the total area under the XES curve. This is a measure of the total number of O p-states in the respective region. The calculated O p DOS for each U value are integrated in the same way. The energy location of the region splitting is based on the energy below the Fermi level that the experimental peaks were split. For instance, the CuO Fermi level was experimentally found to be 529.8 eV, and the peaks were split at 525.4 eV; thus the DOS regions are split at -4.4 eV as shown by the dashed line in Figure 7.6. The TM d-states were integrated the same way as the O p-states. The ratio of the left states over the right states for both TM d and O p-states were plotted as a function of U to observe the trends. The results for all compounds are shown in Figure 7.9. It should be noted that the sensitivity of the choice of the energy at which to separate the regions in the experimental XES was tested. When the energy was shifted by 0.2 eV in either direction (up or down in energy), the trend of the ratios did not change. The ratios were shifted up slightly when the separation was done 0.2 eV higher in energy, and down slightly when it was shifted lower in energy. This is the expected effect of altering the point at which the regions are separated.

The trend of the O p ratio is quite linear for all compounds, except CuO which shows more of a decaying exponential trend. All of the TM d ratios have an increasing exponential trend, except Cu_2O which is very linear until high U when it increases exponentially as well. It would be quite significant if all compounds shared the same trend with respect to the O p ratios. If so, one could fit a curve, a line for instance, and use the line as a metric to gauge which U value would be appropriate for a similar TMO based on the ratio of the integrated areas of the two peaks in an oxygen XES spectra. This would give a starting point for the level of correlation and a U value to use in calculations and theoretical models. It would provide a much narrower range of U to investigate rather than the large range considered in this research. Computational costs would be reduced significantly. Unfortunately, a single function can not be fit reasonably to all compounds studied here. Although the O p ratios of AgO, Ag_2O, and Cu_2O are all linear, and CuO is quite linear in the range between 2 – 10 eV, the parameters of a fitted line to each compound are not the same. A line was fit for all

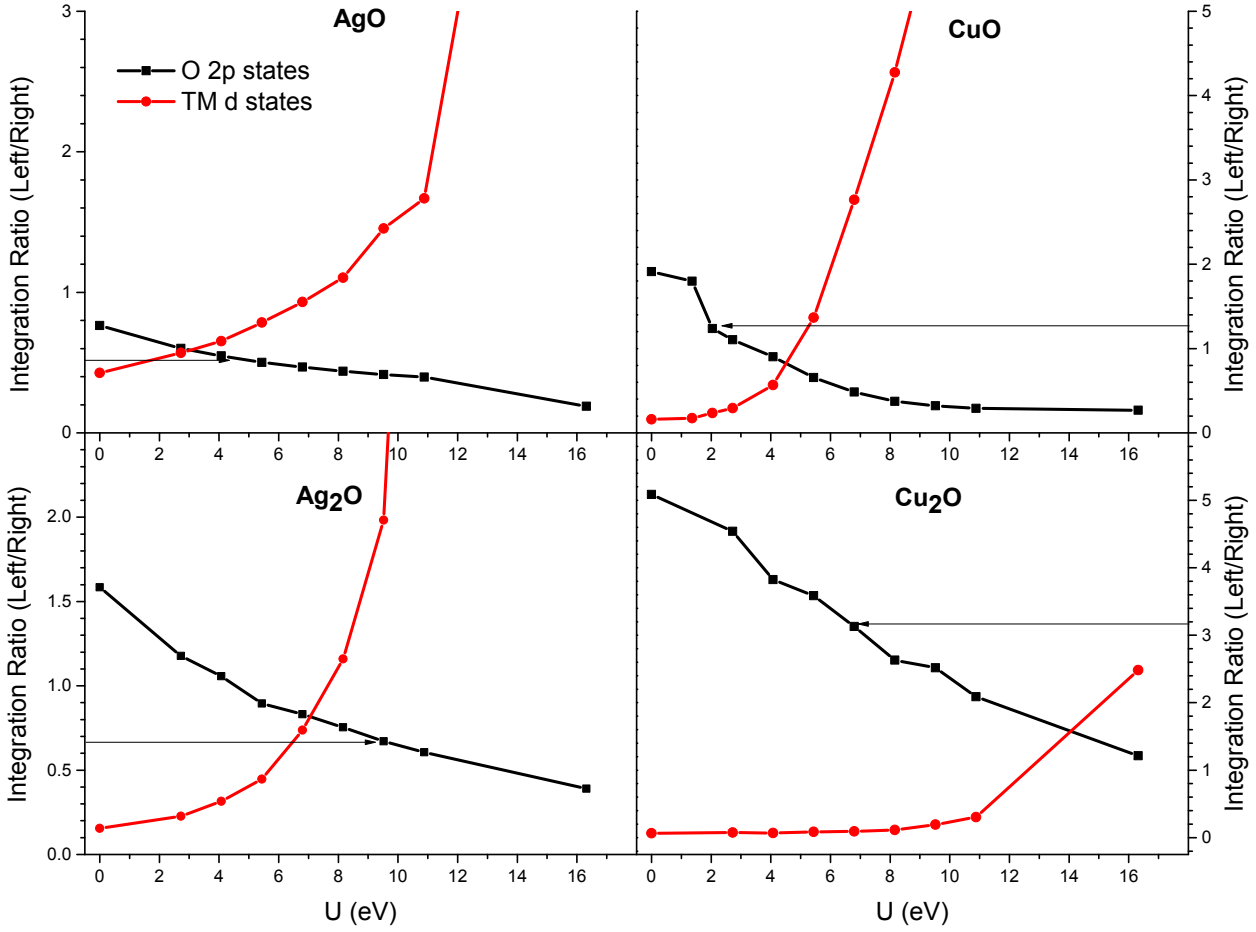

Figure 7.9: Integration Ratios of States vs. U. The ratio of the pDOS in the left region divided by the pDOS in the right region are plotted as a function of U. The arrows represent the ratio derived from the experimental XES as discussed in the text.

compounds, including CuO, using all data points between 0 - 16.3 eV. The fit parameters are shown in Table 7.1.

Clearly, there is no single line that can be fit to all the compounds. The slopes and intercepts vary by almost a full order of magnitude. This line of inquiry seems to be a dead end. Other TMOs, CdO and ZnO, were tested in the same fashion and failed to agree with any of the values above; the fit parameters can be found in Appendix A, Table A.3. However, there is another trend that could be investigated in future research. This is the response to even higher values of U used here. It appears that the O p ratio for CuO may decay asymptotically to some value slightly above zero. It is possible that the other compounds would behave similarly if higher U values were considered. This "saturation" effect, where

Table 7.1: Line fitting parameters for the ratio of left-to-right O p-states.

Compound	Intercept	Slope (eV^{-1})	R-Squared
AgO	0.711±0.021	-0.0320±0.0022	0.96
CuO	1.50±0.16	-0.115±0.026	0.72
Ag_2O	1.386±0.075	-0.0691±0.0083	0.90
Cu_2O	4.94±0.13	-0.252±0.027	0.97

increasing U past a certain value would no longer change the ratio of O p-states in the left and right regions, could be a common feature. Would this asymptotic value be the same or similar for all compounds? Would the ratio tend to zero or some other value slightly above zero? The answer to these questions may provide important understanding of how the +U term added to only the TM d-states affects the oxygen states indirectly.

Another feature to investigate is how the states in the entire valence band respond to the U value. The valence band is not split into regions in this case, rather the entire upper valence band (from about -12 – 0 eV) is integrated and the centroid of the TM d and O p-states are determined and plotted as a function of U. This was done for all compounds and the results are shown in Figure 7.10.

There is clearly a linear response of the centroids to the applied U. The O p and TM d centroids shift up and down respectively in energy as U is increased, as expected. Lines were fit to these plots as well and the fit parameters are listed in Table 7.2. The fits for ZnO and CdO are in Appendix A, Table A.4 for comparison.

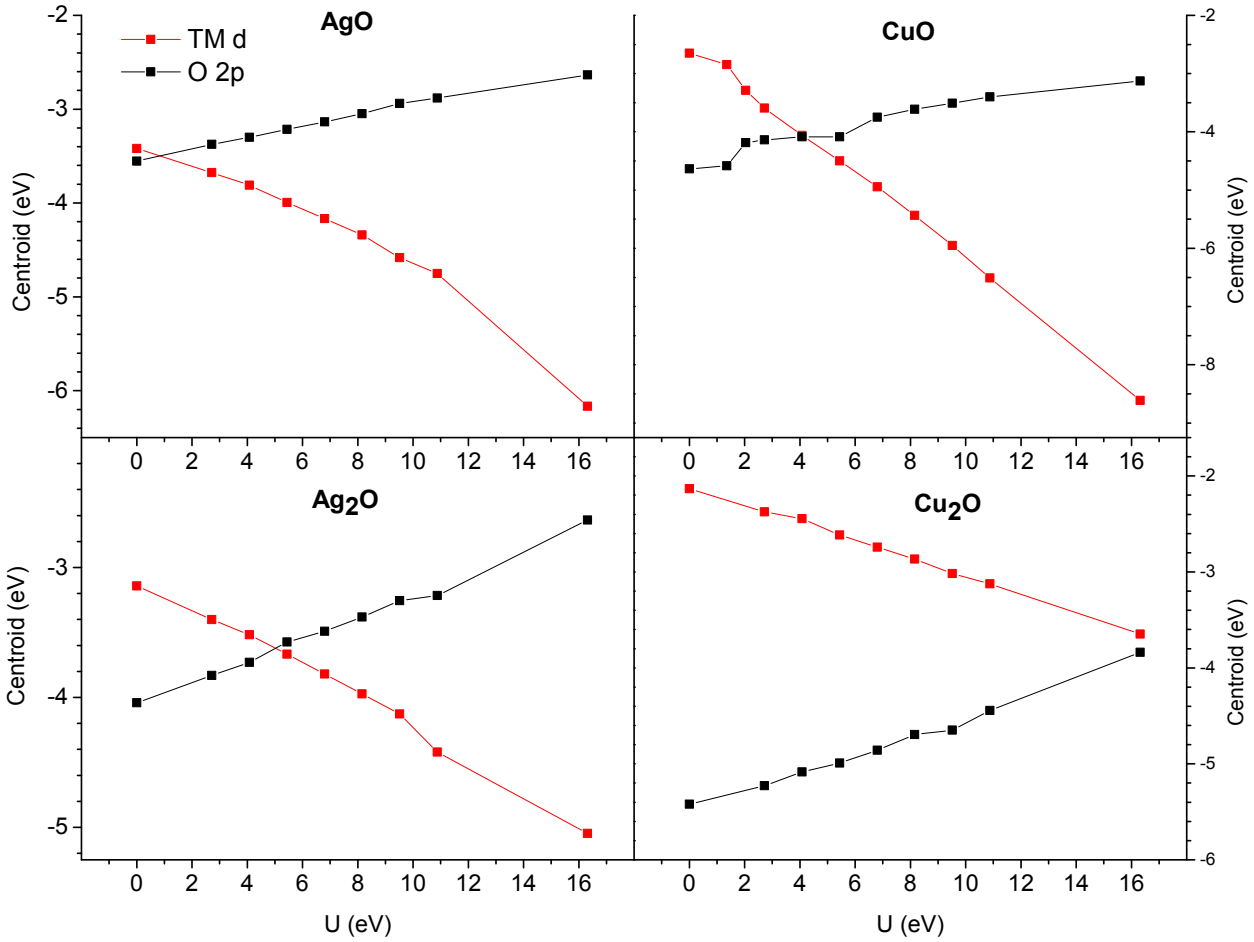

Figure 7.10: Centroids of TM *d* and O *p*-states in the valence band vs. U.

Table 7.2: Line fitting parameters for the valence band centroid of O *p* and TM *d*-states.

Compound	O *p*			TM *d*		
	Intercept (eV)	Slope	R-Squared	Intercept (eV)	Slope	R-Squared
AgO	-3.528±0.017	0.0574±0.0020	0.99	-3.16±0.12	-0.163±0.015	0.94
CuO	-4.504±0.068	0.0956±0.0088	0.92	-2.512±0.047	-0.3679±0.0062	0.997
Ag_2O	-4.062±0.022	0.0846±0.0026	0.99	-3.058±0.037	-0.1188±0.0044	0.99
Cu_2O	-5.488±0.031	0.0967±0.0037	0.99	-2.107±0.013	-0.0939±0.0016	0.998

The fits are all very good; the R-squared values are very high. The intercepts are not of much interest, but the slopes are. The responses of Ag_2O and Cu_2O are quite similar; the slope values of both d and p centroids are similar between the compounds. The slopes of the d and p centroids are very similar to each other for each compound as well. CuO has the steepest response of the d-states, Ag_2O and Cu_2O have the lowest magnitude, and AgO has a magnitude in the intermediate range. It is interesting that the slope values of the d-centroids are so small. In a simple Hubbard model the valence states are shifted down in energy by U/2 and the conduction band states are shifted up by U/2 [25]. In this model the slopes would have a value of -0.5 eV/eV. Only CuO has a value that is reasonably close to this; the others are much lower. This is further evidence that the simple Hubbard model is not sufficient to model these TMOs. A certain amount of band character is needed in the model as well. There could be meaningful information derived from the response of the valence states to the added U term. Is the fact that Ag_2O and Cu_2O are isostructural and have similar responses significant? Is there physical meaning to the fact that the TM d and O p slopes are similar in magnitude for both these compounds? Why does CuO have a much greater slope magnitude than the others? The response of the O p centroids is similar for all compounds; is this significant? These questions are a good starting point for further research.

Chapter 8

Bandgaps and Measurable Quantities

Several important quantities of interest to condensed matter physics can be extracted from X-ray spectroscopy and DFT calculations. The bandgap of a material is a critical quantity for the development of transistors, solar cells, batteries, and other electronic applications. An estimate of the charge transfer energy discussed in section 3.5 can be obtained from X-ray spectra. The charge transfer energy is defined as the energy difference between the highest lying oxygen $2p$ state and the lowest lying metal $3d$-state. The highest energy O p-state can be read from the highest peak in the O XES spectra, and the lowest metal $3d$-state can be approximated as the lowest energy peak in O XAS. This approximation is reasonable since the calculated DOS show that the lowest conduction band states are hybridized O p - metal d-states, thus the metal d-states in this region can be considered at the same location as the O p-states. This method has been shown to produce accurate results for other TMOs [35]. An estimate of the core-hole effect can be determined from core-hole calculations as discussed in section 4.3. Unfortunately, there is no proven reliable method for extracting the U_{dd} Coulomb energy in TMOs from oxygen XES and XAS . Photoelectron, Auger electron, and bremsstrahlung isochromatic spectroscopies (BIS) can be used to estimate U_{dd} however [41]. DFT calculations suffer from an inherent "derivative discontinuity" problem that leads to the severe underestimate of calculated bandgaps [19]. Some functionals such as MBJ perform better than others in this respect, but any estimates from DFT calculations should not be expected to be accurate.

8.1 Bandgaps

The experimentally determined bandgaps were based on the second-derivative method mentioned in chapter 5. The second-derivatives of all four compounds are shown in Figure 8.1. The calculated values along with previously reported values are shown in Table 8.1.

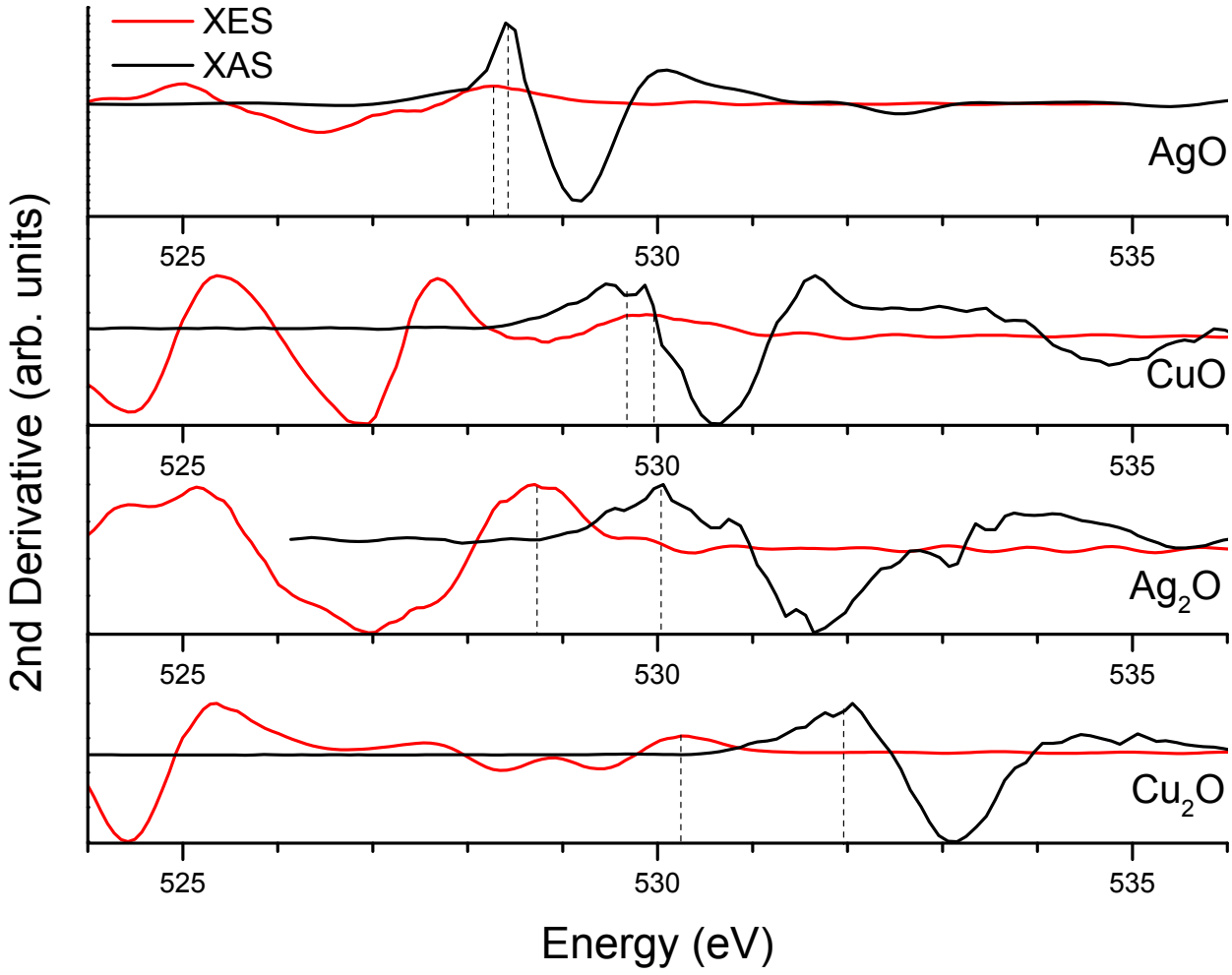

Figure 8.1: Second-derivatives of XES and XAS. The dotted lines represent location of the peaks used to determine the bandgap.

The PBE functional underestimates bandgaps for all compounds as expected. CuO is incorrectly predicted to be metallic, and the others are well below their expected values. MBJ does improve in most cases but still predicts bandgaps that are about half of the known values. Adding and increasing the U value slowly increases the bandgaps of all compounds;

Table 8.1: Calculated, measured, and previously reported bandgaps. Estimates of errors in the experimental gaps are reported in brackets.

						PBE+U (eV)						
Compound	PBE	MBJ	HF	MBJ+U=4.0 eV	HSE	4.0	5.4	6.8	8.2	9.5	Exp.	Literature
Cu_2O	0.62	0.94	0.94	1.1	2.01	0.80	0.86	0.90	0.95	0.99	1.75(0.3)	2.2 [50], 2.4 [41]
CuO	0	0	1.6	4.1		1.67	1.74	1.75	1.77	1.78	0(0.5)	1.4 [41], 1.9 [46]
Ag_2O	0.15	0.73	0.26	0.95	1.26	0.26	0.27	0.30	0.33	0.36	1.35(0.3)	1.3 [50], 1.46 [54]
AgO	0.09	0.40	0.39	0.71		0.27	0.34	0.41	0.48	0.56	0.15(0.3)	1.0 [44], 1.1 [55]

for CuO the inclusion of a +U term gets the bandgap within the range of accepted values. The HSE functional is very accurate for Ag_2O and Cu_2O. The second-derivative method performs well for Ag_2O and Cu_2O but fails for AgO and CuO. In summary, there is no single functional that performs best across the spectrum of compounds studied here. HSE is the most accurate, but unfortunately HSE calculations for AgO and CuO could not be carried out due to technical difficulties.

8.2 Core-hole Effect

It has been shown previously that the oxygen $1s$ XAS is not strongly effected by the core-hole in TMOs [35, 56]. The general effect should be to lower the energy of the unoccupied states slightly, without significantly altering the features of the spectra. The core-hole XAS shown in chapter 6 show that the features and shape of the spectra for all compounds do not change, but are shifted slightly to lower energy. The core-hole effect can be estimated by comparing calculations with and without the core-hole accounted for. The calculated bandgap is added to the Fermi energy to determine the onset energy of the conduction band for each calculation. The difference between the two onset energies gives an estimate of the core-hole shift

$$CH_{Shift} = (FE_{NCH} + BG_{NCH}) - (FE_{CH} + BG_{CH}) \tag{8.2.1}$$

where FE is the Fermi energy, BG is the bandgap, NCH refers to the non-core-hole calculation, and CH the calculation including the core-hole. The estimated shifts for all compounds

Table 8.2: Estimated core-hole shifts.

Compound	Core-hole Shift (eV)
AgO	0.063
CuO	-0.002
Ag_2O	0.336
Cu_2O	0.079

are reported in Table 8.2. The fact that CuO has a negative shift is somewhat surprising; however, in this case, both the core-hole and non-core-hole calculation have zero bandgap, and the Fermi energy for the core-hole calculation is slightly above that of the non-core-hole calculation. AgO and Cu_2O have negligible shifts, and even Ag_2O is very small. Thus, the core-hole effect is proven to be very small in these TMOs, consistent with previous findings. Examining the DOS and the XAS of the core-hole calculation, we see that the general effect of the core hole was to increase the DOS at the lower energy region of the conduction band without changing the onset energy. This same effect has been reported in similar oxides [56].

8.3 Charge Transfer and On-site Coulomb Energies

The charge transfer energy can be approximated as discussed above, but the on-site Coulomb interaction (U_{dd}) unfortunately cannot be estimated from XES and XAS spectra. The values are reported in Table 8.3 along with available values from the literature. There is good agreement of charge transfer energy for CuO, but the estimated values for Ag_2O and Cu_2O are much higher than the literature values. All of the reported U_{dd} values are higher than the estimated and reported charge transfer energies. Therefore, CuO, Ag_2O, and Cu_2O would be classified as charge transfer type insulators in the Zaanen-Sawatzky-Allen scheme [34]. AgO is expected to have a similar on-site Coulomb energy as Ag_2O and, thus, would also be a charge transfer type insulator [57].

Table 8.3: Charge transfer and Coulomb energies.

Compound	$\Delta_c^{est} \pm 1.0$	Δ_c^{Lit}	U_{dd}^{Lit}
AgO	2.5		
CuO	2.2	2.2 [41], 3.2 [58]	6.5 [58]
Ag_2O	4.8	1.3 [50]	5.8 [50]
Cu_2O	4.2	1.7 [50]	9.3 [41], 9.2 [50]

Chapter 9

Conclusions

9.1 Functional Models

The results of the functional analysis, chapter 6, show that an inclusion of a +U term in the exchange-correlation functional is needed for all of these TMOs. This is not surprising as these are all *d*-electron systems and are expected to be quite highly correlated. What is somewhat surprising is that the PBE functional without an added U term performs as well as it does. The calculated X-ray spectra with the PBE functional is in very good agreement with experimental spectra for AgO and Cu_2O, although not as good for CuO and certainly not for Ag_2O. The HSE functional performs well for Cu_2O and equally as well as PBE for Ag_2O. The fact that the bandgaps are very accurate with the HSE functional along with the relatively good agreement with experimental spectra, makes HSE a promising functional for these types of systems. HSE calculations for CuO and AgO could be valuable and should be the subject of further research.

9.2 The Effects of the Hubbard U Term

Adding a +U term to an exchange-correlation functional serves to localize the TM *d*-electrons to the host atom. Doing so increases the binding energy of these electrons shifting them further from the Fermi level. It is apparent that shifting the *d*-states has an affect on the O *p*-states as well, which is to shift them closer to the Fermi level. This effect can be seen in the oxygen XES as the shifting of intensity to the peak at higher energy (closer to the Fermi level) and lowering intensity in the lower energy peak. The U value which optimizes the peak ratios of the emission spectra was determined for each compound. AgO was determined

to be optimized by U=4.0 – 5.5 eV, in agreement with previously reported values. CuO and Cu_2O was optimized by U=2.0 eV and U=4.0 – 5.5 eV, respectively; both values are lower than reported values of around 7.5 eV for similar copper-oxide systems. Ag_2O was optimized by U=9.5 eV; there are no known values in the literature for comparison.

The peak ratios of the experimental and calculated XES were used in an attempt to create a metric with which to predict appropriate U values for similar systems. The peak ratios as a function of U showed a near linear trend for all compounds. From this, lines were fit with hopes of using the parameters of the line as the metric. Unfortunately, there was not agreement between the parameters of the lines for all compounds. Thus, this metric would not be widely applicable to this class of materials, but would be system-dependent and not a valuable predictive tool as hoped. However, there are some trends that appear in the data that could be of interest. The asymptotic trend at high U values shown by CuO could be common to all these compounds if calculations with higher U values were performed. It may be significant if all compounds tended to the same ratio, or if there were a common "saturation" value of U. Also, the behaviour of the centroid of the total valence band *d* and *p* states is interesting. The O *p* centroid responds very similarly in all compounds despite the fact that the TM *d*-states respond differently. What can be derived from the centroid shifts about the *p*-*d* repulsion in these systems? The centroid of a certain state is common in all materials; every TMO will have a TM *d* and O *p* centroid in the valence band. Might there be system-wide correlations in the centroid shifts? Can a metric be derived based on the centroids rather than the system-dependent peak ratios? These questions could be the focus of future research; the answers may provide important insight into the nature of transition metal oxides and *d*-electron systems in general.

References

[1] J. Stöhr and H. C. Siegmann. *Magnetism: From Fundamentals to Nanoscale Dynamics*, volume 152 of *Springer Series in Solid-State Sciences*. Springer, New York (2006).

[2] J. Pan, Y. Sun, Z. Wang, P. Wan, X. Liu and M. Fan. J. Mater. Chem. **17** 4820 (2007).

[3] H. Li, Y. Wang, P. He and H. Zhou. Chem. Commun. **46** 2055 (2010).

[4] H. Takahashi, N. Rikitake, T. Sakuma and Y. Ishii. Solid State Ionics **168** 93 (2004).

[5] D. Dellasega, A. Facibeni, F. D. Fonzo, M. Bogana, A. Polissi, C. Conti, C. Ducati, C. S. Casari, A. L. Bassi and C. E. Bottani. Nanotechnology **19** 475602 (2008).

[6] S. Yonezawa and Y. Maeno. Phys. Rev. B **72** 180504 (2005).

[7] S. Bennici, A. Gervasini and V. Ragaini. Ultrasonics Sonochemistry **10** 61 (2003).

[8] E. Manousakis. Rev. Mod. Phys. **63** 1 (1991).

[9] V. Fock. Z. Physik **61** 126 (1930).

[10] P. Hohenberg and W. Kohn. Phys. Rev. **155** B864 (1964).

[11] S. Cottenier. Density Functional Theory and the Family of (L)APW-methods: a step-by-step introduction. Instituut voor Kern- en Stralingsfysica, K.U.Leuven, Belgium (2002).

[12] W. Kohn and L. J. Sham. Phys. Rev. **140** A1133 (1965).

[13] J. Harris. Phys. Rev. A **29** 1648 (1984).

[14] J. P. Perdew. Phys. Rev. Lett. **55** 1665 (1985).

[15] J. P. Perdew and Y. Wang. Phys. Rev. B **45** 13244 (1992).

[16] J. P. Perdew, K. Burke and M. Ernzerhof. Phys. Rev. Lett. **77** 3865 (1996).

[17] F. Tran, P. Blaha, K. Schwarz and P. Novák. Phys. Rev. B **74** 155108 (2006).

[18] R. M. D. Engel Eberhard. *Density Functional Theory: An advanced Course*. Springer (2011).

[19] J. P. Perdew and M. Levy. Phys. Rev. Lett. **51** 1884 (1983).

[20] V. I. Anisimov, J. Zaanen and O. K. Andersen. Phys. Rev. B **44** 943 (1991).

[21] V. I. Anisimov, I. V. Solovyev, M. A. Korotin, M. T. Czyżyk and G. A. Sawatzky. Phys. Rev. B **48** 16929 (1993).

[22] M. T. Czyżyk and G. A. Sawatzky. Phys. Rev. B **49** 14211 (1994).

[23] L. Wang, T. Maxisch and G. Ceder. Phys. Rev. B **73** 1 (2006).

[24] P. Novák, J. Kuneš, L. Chaput and W. E. Pickett. Phys. Stat. Solidi B **243** 563 (2006).

[25] V. I. Anisimov, F. Aryasetiawan and A. I. Lichtenstein. J. Phys.: Cond. Matt. **9** 767 (1997).

[26] O. Gunnarsson, O. K. Andersen, O. Jepsen and J. Zaanen. Phys. Rev. B **39** 1708 (1989).

[27] A. D. Becke. J. Chem. Phys. **98** 5648 (1993).

[28] J. Heyd, G. E. Scuseria and M. Ernzerhof. J. Chem. Phys. **118** 8207 (2003).

[29] A. D. Becke and E. R. Johnson. J. Chem. Phys. **124** 221101 (2006).

[30] F. Tran and P. Blaha. Phys. Rev. Lett. **102** 5 (2009).

[31] J. P. Allen, D. O. Scanlon and G. W. Watson. Phys. Rev. B **81** 1 (2010).

[32] F. Tran and P. Blaha. Phys. Rev. B **83** 235118 (2011).

[33] J. Hubbard. Proceedings of the Royal Society of London Series A-Mathematical and Physical Sciences **276** 238 (1963).

[34] J. Zaanen, G. A. Sawatzky and J. W. Allen. Phys. Rev. Lett. **55** 418 (1985).

[35] E. Z. Kurmaev, R. G. Wilks, A. Moewes, L. D. Finkelstein, S. N. Shamin and J. Kuneš. Phys. Rev. B **77** 165127 (2008).

[36] E. McDermott. *Study of Solid State Photocatalysts and Other Energy Materials using Synchrotron Radiation.* Master's thesis, University of Saskatchewan (2012).

[37] P. Blaha, K. Schwarz, G. K. H. Madsen, D. Kvasnicka and J. Luitz. *WIEN2k, An Augmented Plane Wave + Local Orbitals Program for Calculating Crystal Properties.* Karlheinz Schwarz, Techn. Universität Wien, Austria (2001). ISBN 3-9501031-1-2.

[38] S. Åsbrink and L.-J. Norrby. Acta Crys. B **26** 8 (1970).

[39] M. Jansen and P. Fischer. J. Less Common Metals **137** 123 (1988).

[40] P. Norby, R. Dinnebier and A. N. Fitch. Inorg. Chem. **41** 3628 (2002).

[41] J. Ghijsen, L. Tjeng, J. V. Elp and H. Eskes. Phys. Rev. B **38** 322 (1988).

[42] J. Perdew, K. Burke and M. Ernzerhof. Phys. Rev. Lett. **77** 3865 (1996).

[43] J. A. McLeod, N. A. Skorikov, L. D. Finkelstein, E. Z. Kurmaev and A. Moewes. J. Phys. Chem. C **116** 24248 (2012).

[44] N. R. C. Raju, K. J. Kumar and A. Subrahmanyam. J. Phys. D: App. Phys. **42** 135411 (2009).

[45] J. P. Allen, D. O. Scanlon and G. W. Watson. Phys. Rev. B **84** 1 (2011).

[46] S. C. Ray. Solar Energy Materials and Solar Cells **68** 307 (2001).

[47] J.-M. Mariot, V. Barnole, C. F. Hague, G. Vetter and F. Queyroux. Z. Phys. B Cond. Matt. **75** 1 (1989).

[48] A. Gordienko, Y. Zhuravlev and D. Fedorov. Phys. Solid State **49** 223 (2007).

[49] P. Marksteiner, P. Blaha and K. Schwarz. Z. Phys. B Cond. Matt. **127** 119 (1986).

[50] L. Tjeng, M. Meinders and J. V. Elp. Phys. Rev. B **41** 3190 (1990).

[51] J. Bednorz and K. Müller. Z. Phys. B Cond. Matt. **64** 189 (1986).

[52] V. I. Anisimov, J. Zaanen and O. K. Andersen. Phys. Rev. B **44** 943 (1991).

[53] N. Mosey and E. Carter. Phys. Rev. B **76** 155123 (2007).

[54] Y. Ida, S. Watase, T. Shinagawa, M. Watanabe, M. Chigane, M. Inaba, A. Tasaka and M. Izaki. Chem. Mat. **20** 1254 (2008).

[55] B. E. Breyfogle, C. Hung, M. G. Shumsky and J. A. Switzer. J. Electrochemical Soc. **143** 2741 (1996).

[56] J. A. McLeod, R. G. Wilks, N. A. Skorikov, L. D. Finkelstein, M. Abu-Samak, E. Z. Kurmaev and A. Moewes. Phys. Rev. B **81** 245123 (2010).

[57] K. Park. Phys. Rev. B **49** 4425 (1994).

[58] R. Zimmermann and P. Steiner. J. Phys.: Cond. Matt. **11** 1657 (1999).

Appendix A

Appendix

Table A.1: XES calibration standards.

Element	Emission Line	Calibration Material	Energy Peak
O	K α	$Bi_4Ge_3O_{12}$	526.0 eV *

Table A.2: XAS calibration standards.

Element	Absorption Spectrum	Calibration Material	Energy Peak
O	O 1s	$Bi_4Ge_3O_{12}$	532.7 eV *

* $Bi_4Ge_3O_{12}$ (BGO) features were calibrated against elastically scattered peaks measured at the ALS Beamline 8.0.1 spectrometer.

Table A.3: Line fitting parameters for the ratio of left-to-right O *p*-states in CdO and ZnO.

Compound	Intercept	Slope (eV^{-1})	R-Squared
ZnO	0.229±0.014	-0.0116±0.0016	0.90
CdO	0.0990±0.0061	-0.00506±0.00068	0.90

Table A.4: Line fitting parameters for the valence band centroid of O *p* and TM *d*-states in CdO and ZnO

Compound	O *p*			TM *d*		
	Intercept (eV)	Slope	R-Squared	Intercept (eV)	Slope	R-Squared
ZnO	-2.873±0.025	0.0502±0.0027	0.98	-4.066±0.054	-0.3015±0.0061	0.997
CdO	-2.286±0.018	0.0385±0.0021	0.98	-6.061±0.034	-0.3313±0.0038	0.9992